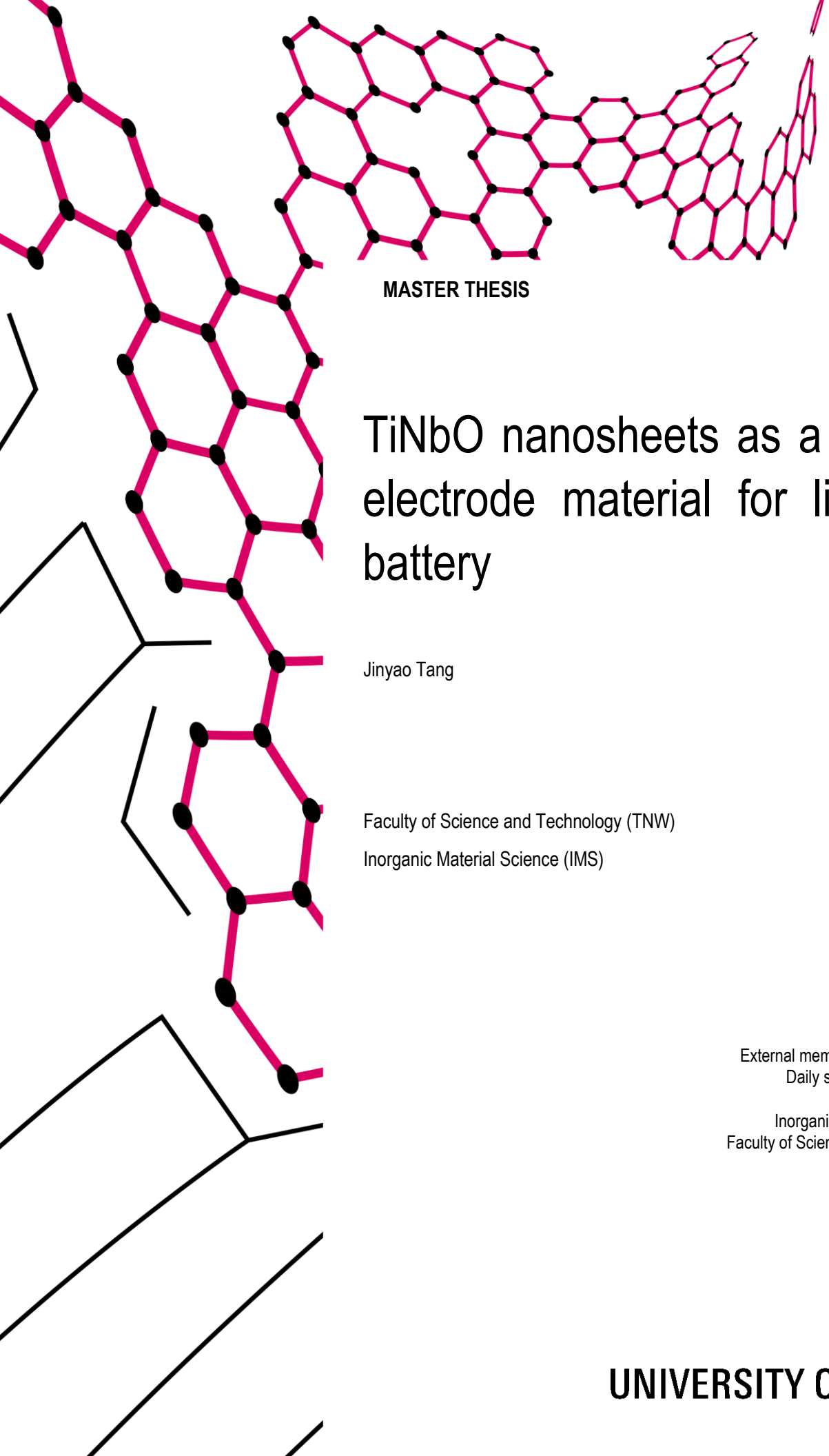

MASTER THESIS

TiNbO nanosheets as a high-rate electrode material for lithium-ion battery

Jinyao Tang

Faculty of Science and Technology (TNW)

Inorganic Material Science (IMS)

Supervisor:
Prof. dr. ir. J. E. ten. Elshof
External member: Prof. dr. ir. M. Huijben
Daily supervisor: R. Xia, J. Zheng

Inorganic Materials Science Group,
Faculty of Science and Technology (TNW)
Chemical Engineering
University of Twente
P.O. Box 217
7500 AE Enschede
The Netherlands

UNIVERSITY OF TWENTE.

Abstract

Lithium-ion batteries have been widely used in mobile electronic equipment, electrical vehicles, and smart energy storage terminals because of their high energy density and good cycle stability. The anode material is an important factor in the performance of lithium ion batteries. However, as the above-mentioned equipment further increases the requirements for the endurance and charging time of lithium-ion batteries, the current commercial graphite-based carbon anode materials can no longer meet the demand.

Titanium niobate oxides (TNO) has a high theoretical specific capacity, and the unit cell volume changes little during the deintercalation process of lithium ions so that the reversibility is high. Therefore, it is a new type of high-performance anode material with considerable application prospects. However, its inherently low ionic and electronic conductivity limits the improvements of its electrochemical performance. In this thesis, the TNO ($TiNbO_5$ and Ti_5NbO_{14}) was exfoliated into nanosheets and compared with HTNO bulks.

First, the exfoliation process of $TiNbO_5$ nanosheets was optimized by comparing the capacity performance of the nanosheets fabricated by previous procedure and the optimized one. The rate charge-discharge test results shows the optimized nanosheets had over 50 mAh/g at 20C, which is higher than the older one. The optimized method is to dry the protonated powder at room temperature overnight and neutralize the exfoliation solution with acid. The nanosheets are obtained by being washed and dried at room temperature in a vacuum oven.

Second, the exfoliation condition of Ti_5NbO_{14} nanosheets was explored. The nanosheets exfoliated at different conditions were deposited on a Si substrate by Langmuir-Blodgett deposition and characterized by Atomic force microscopy. The most efficient exfoliation condition is to mix 0.4g $H_3Ti_5NbO_{14}$, 2.11 mL TBAOH and 80 mL deionized water to react for 24 hours.

After that, the $TiNbO_5$ nanosheets, Ti_5NbO_{14} nanosheets, $HTiNbO_5$ bulk and $H_3Ti_5NbO_{14}$ bulk were characterized by X-ray diffraction and Scanning electron microscopy to analyze the crystal lattice and morphology of the research objectives. It can be seen the nanosheets samples have fluffy layered structures which lead to a larger inner area.

Finally, the electrochemical characterization was carried on the four active materials for rate charge-discharge test, cyclic voltammetry, electrochemical impedance spectroscopy and long cycling test. The results show the $HTiNbO_5$ bulk had best performance among the four materials with highest lithium ion diffusion coefficient and contribution of pseudocapacitance. The nanosheets with Ti : Nb ratio of 1 : 1 perform better than nanosheets with 5 : 1 ratio, while same results show in bulk samples. The reason is that Nb^{5+}/Nb^{4+} redox reaction is controlled reaction in the whole process, and the samples with higher Nb percentage have better lithium ion diffusion ability with a result of higher specific capacity. The nanosheets samples are not good as expected due to their fluffy layered structure and their inner area cannot be coated with the carbon black so that the conductivity is affected and the capacity is lower than expected.

Key words: Lithium ion batteries, Anode materials, $TiNbO_5$ nanosheets, Ti_5NbO_{14} nanosheets, $HTiNbO_5$ bulk, $H_3Ti_5NbO_{14}$ bulk, Exfoliation.

Acknowledgement

Firstly, I would like to thank Professor ten Elshof for his supervision. My master thesis was successfully completed under his careful guidance. Thanks for Rui Xia and Jie Zheng for their daily supervision especially their help for Langmuir-Blodgett deposition and XRD. The design of the experiments was done with their help and guidance. Also, I have to thank Professor Mark Huijben as external member of committee, Daniel Monteiro Cunha for the introduction of AFM, Karin van den Nieuwenhuijzen for the introduction of XRD and Mark Smithers for taking SEM images for my samples.

I also want to express my appreciate to my parents for their both financial and mental supports during these two years in master study. Thank Peixiao Zhao, Ziyang Shen and Juanqiao He due to their everyday companion. Special thanks to Mr. Victor Li, he is the one who accompanies me since 26 Dec 2017. He is always my spiritual support and stands behind me.

Finally I would like to say thank you to everyone who helped and supported me during my study. I am me because of all of you.

Abbreviations

AFM	Atomic force microscopy
CV	Cyclic voltammetry
EIS	Electrochemical impedance spectroscopy
HTNO	$HTiNbO_5$ and $H_3Ti_5NbO_{14}$ bulks
LB	Langmuir-Blodgett
LIB	Lithium ion battery
SEM	Scanning electron microscopy
TNO	Titanate niobium oxide
XRD	X-ray diffraction
C	Concentration of lithium ions
$\mathbf{D_{Li^+}}$	Diffusion coefficient of lithium ions
$\mathbf{i_p}$	Current at peak
$\mathbf{R_b}$	Ohmic impedance
$\mathbf{R_{ct}}$	Transfer impedance of the charge
$\mathbf{R_{sei}}$	Diffusion impedance of lithium ions in solid electrolytes
$\boldsymbol{v}$	Scan rates
W	Warburg impedance

Contents

1 Research background

1.1 Introduction

Due to an exponentially increasing global population and corresponding demand of energy, the transition to renewable energy and energy storage devices is one of the most challenges for humankind in this century. According to the Statistical Review of World Energy 2020 as shown in **Figure 1.1**[1], over 85% of the total consumed energy is still from fossil fuels as oil, coal and natural gas. However, the storage of fossil fuel is decreasing and the emission of harmful gases such as SO_2 and CO_2 cause a series of problems as ocean acidification and global warming. Some renewable energies such as solar energy, tidal energy and nuclear energy are difficult to be widely applied. With this trend, there is an urgent need of energy storage devices for efficient use of renewable energy.

Lithium-ion battery (LIBs) is one of the most convincing energy storage devices, which is widely applied in portable electronic devices and new energy resource vehicles. Li-ion battery has both high energy density, excellent cycle stability, good rate performance and are environmentally friendly. Since the improvement of the specific capacity of electrodes, cycle life of the battery and rate are behind the requirement of the devices nowadays, LIBs research is facing a choke point[2]. Thus, a lithium based micro-battery electrode with high-rate performance and long cycle life is urgently needed for micro-battery application.

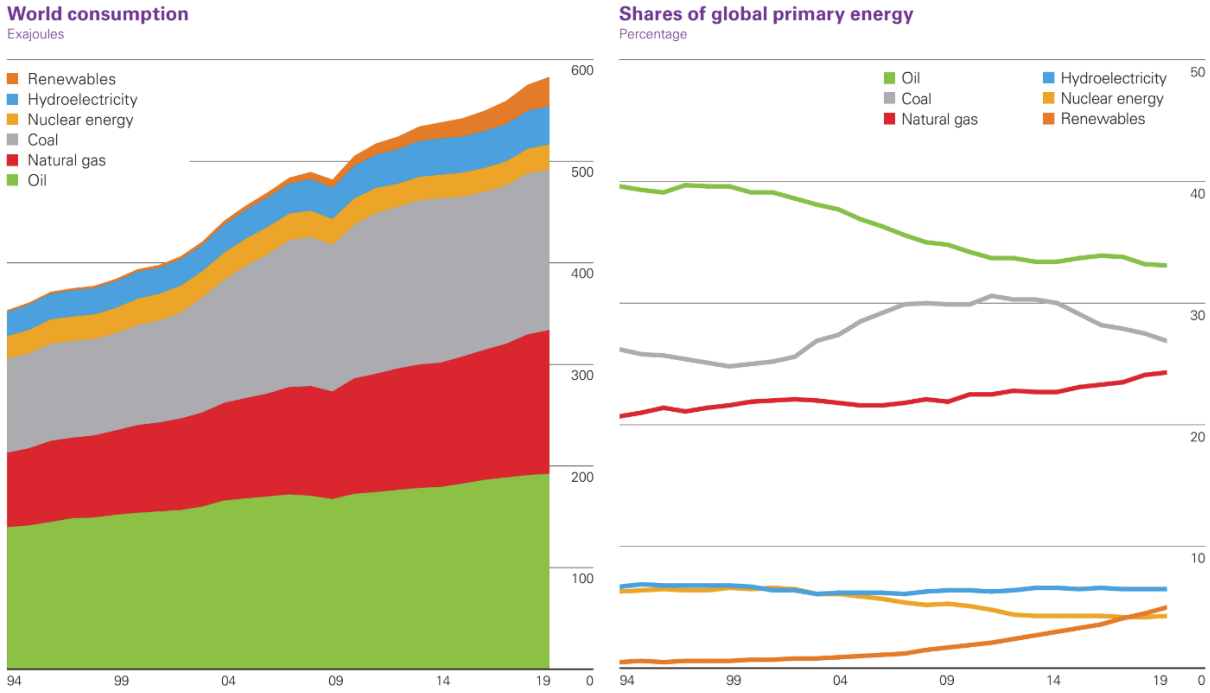

Figure 1.1 Trends of primary energy consumption.[1]

1.2 Lithium-ion battery

Lithium-ion battery (LIB) is now developed into a rechargeable battery in which lithium ion are reciprocally intercalated between anode and cathode and redox reactions occur. Based on primary Li cells invented with Li metal as anode in 1970s, Exxon attempted to produce rechargeable LIB with

TiS_2 as the cathode, Li metal as anode and lithium perchlorate in dioxolane as the electrolyte[3]. However, there were shortcomings of Li-metal/liquid battery system since uneven Li growth(**Figure 1.2a**) during discharge-charge cycle led to explosion hazards[4]. Researchers found a solution to this problem by substituting Li metal with a second insertion material as **Figure 1.2b**, which is so called rocking-chair technology[5,6]. This approach was demonstrated with the commercialized $C/LiCoO_2$ rocking-chair cells brought to market by Sony Corporation[7]. To nowadays, rechargeable LIBs are widely used in energy storage and electrical vehicles.

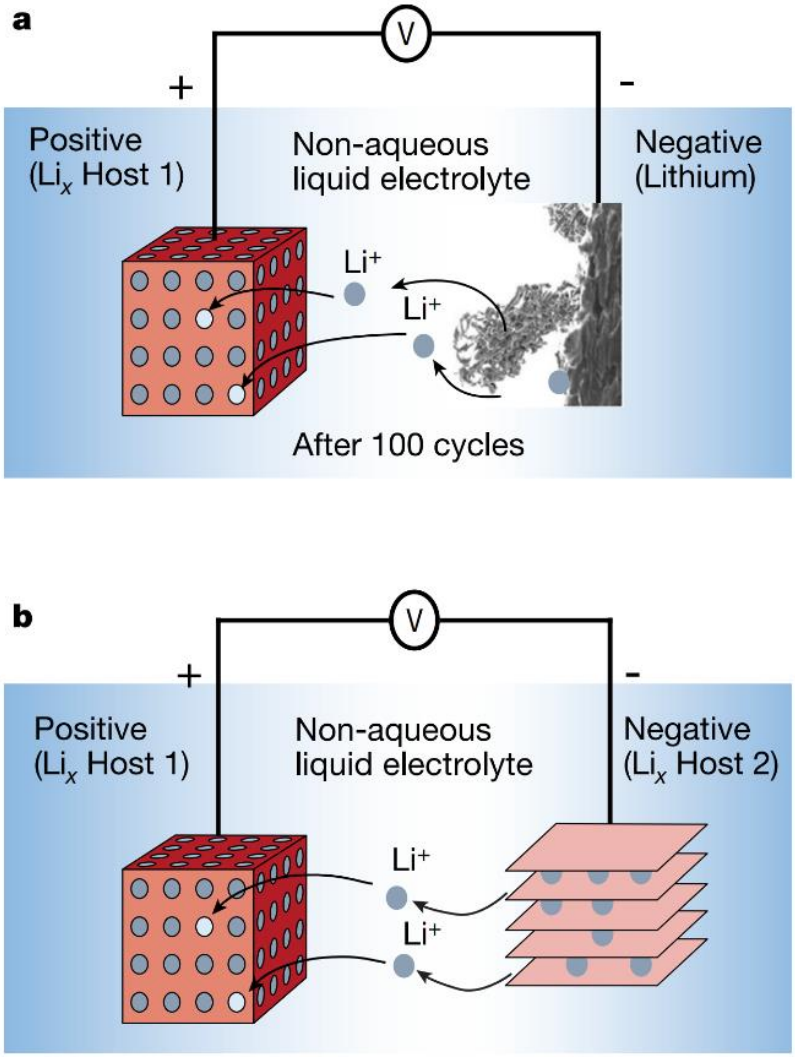

Figure 1.2 Schematic representation and operating principles of Li batteries.[4]

1.2.1 Principle of Lithium-ion battery

The Li-ion battery consists of cathode, anode, separator and electrolyte. The materials for cathode are generally lithium-containing transition metal oxides, such as $LiCoO_2$, $LiMn_2O_4$ and $LiFePO_4$, etc., which are the source of Li ions for the entire LIB. There are many types of anode materials, and commercial LIBs mainly use graphite and lithium titanate. The electrolyte is mainly a solution

composed of a lithium salt and an organic solvent, which can also provided a certain source of Li ion. The separator is a porous polymer membrane, which separates the cathode and anode to prevent short-circuiting due to the contact of the electrodes. The currently used separators are polyolefin microporous membranes.

Figure 1.3 is the schematic diagram of the working principle of LIBs. During charge, driven by the electric field, lithium ions are extracted from the cathode (in the figure it is $Li_{1-x}CoO_2$), migrate toward the anode through the electrolyte, and then intercalate between the graphite layers. This process converts electrical energy into chemical energy stored in the battery. During discharge, lithium ions stored between the graphite layers form Li-ions and migrate back to the cathode, thereby forming a potential difference and a current in the external circuit, realizing the conversion of chemical energy into electrical energy[8].

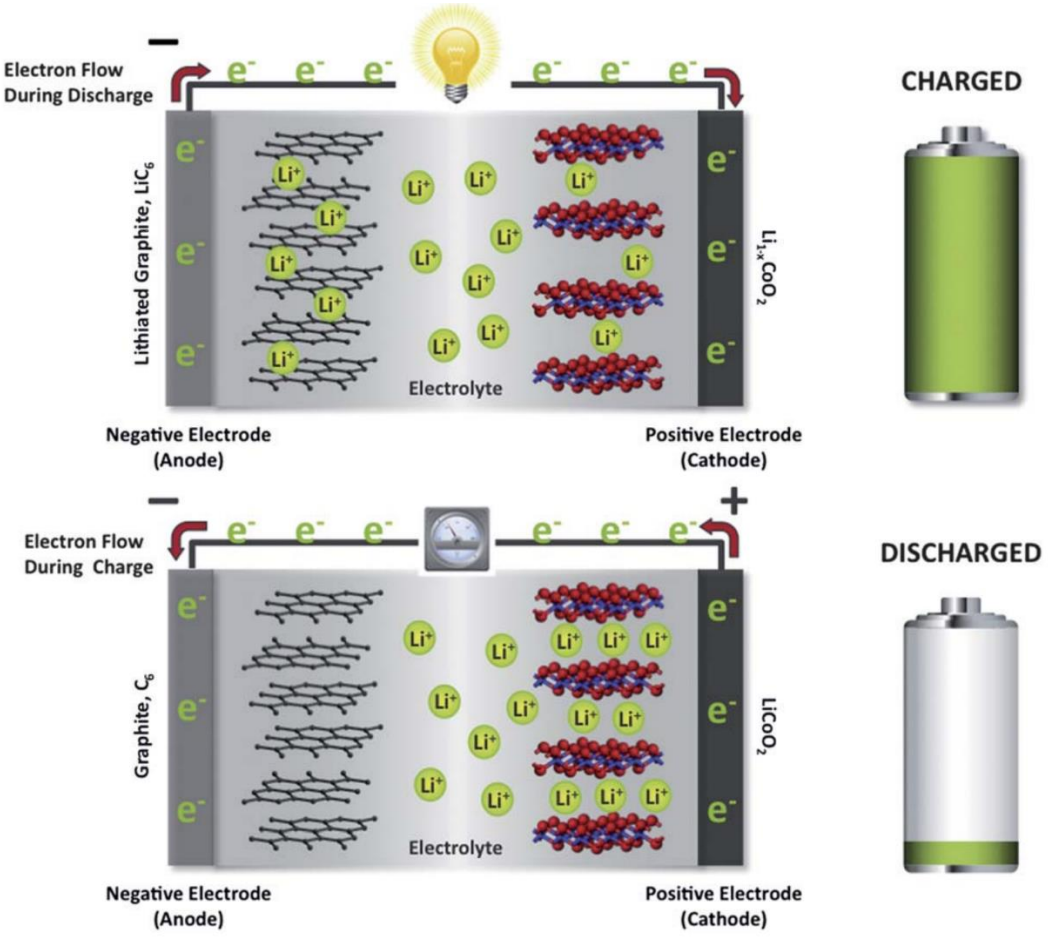

Figure 1.3 A schematic of the working principles of a $Li_xC_6/Li_{1-x}CoO_2$ lithium-ion battery. During discharge, lithium ions diffuse from a lithiated graphite(Li_xC_6) structure (the anode) into a delithiated $Li_{1-x}CoO_2$ structure (the cathode) with concomitant oxidation and reduction of the two electrodes, respectively. The reverse process occur during charge[8].

Comparing with traditional secondary batteries, LIBs have the following advantages[9,10]:

1) High energy density. **Figure 1.4** is a schematic diagram of the comparison between the mass energy density and the volume energy density of the secondary batteries. It can be seen that

the LIB has the highest energy density among the commercial secondary batteries, and its energy density is approximately two to three times to the energy density of Ni-Cd battery and 2 times to that of Ni-MH battery.

2) High working voltage. The working voltage is determined by the materials of cathode and anode. The working voltage of commercial LIB is three times to other secondary batteries. For instance, the working voltage of LIB with $LiCoO_2$ as cathode is around 3.6-3.7V, while those of Ni-Cd and Ni-MH batteries are between 1.5V to 2.0V.
3) Long cycle life. LIB can be cycled for more than 600-1000 times, which is 2.5-10 times that of lead-acid battery(150-400 times).

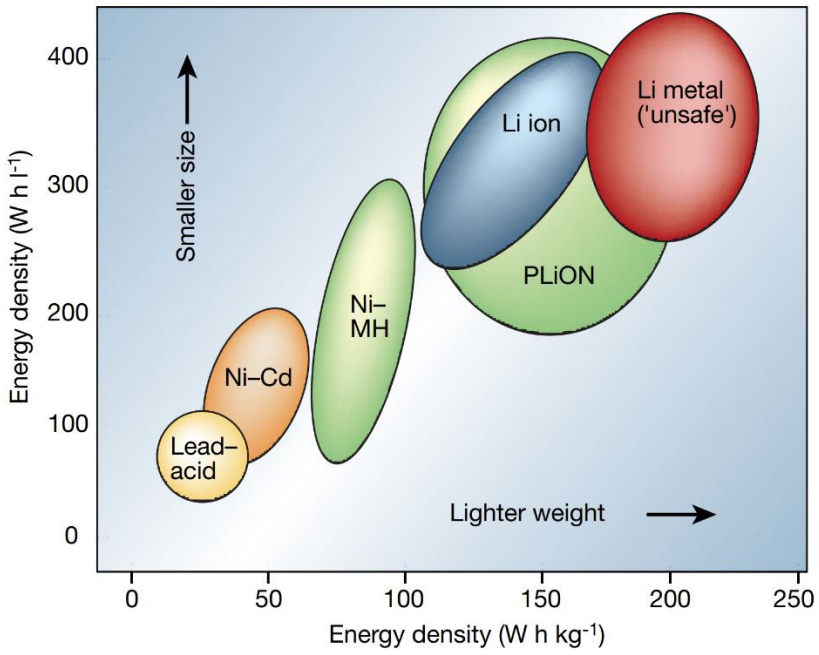

Figure 1.4 Comparison of the various batteries of volumetric and gravimetric energy density[4].

4) Low self-discharge and no memory affect. The monthly self-discharge rate of LIB is only 6-8%, while those of Ni-Cd battery and Ni-MH battery are as high as 20% and 30% respectively and they have certain memory effect. For LIB, its memory affect is almost zero, therefore it can be repeatedly charge and discharge.
5) Wide range of working temperature. The range of the working temperature of LIB is from 20℃ to 45℃.
6) Environmentally friendly. Compared with lead-acid and Ni-Cd batteries which have poison materials, LIB is a green and environmentally friendly battery.

1.2.2 Performance and calculation of lithium ion battery

As an electrochemical energy storage chemical reaction, it usually contains two reactants, and a charge transfer occurs between the two reactants in the process of the reaction. The standard Gibbs free energy of this reaction ($\Delta_r G^\theta$) can be calculated for the electrochemical energy storage capacity with the Gibbs free energy of the reactants and products. If the Gibbs free energy is negative, the reaction proceeds in the direction of the formula.

$$\alpha A + \beta B \rightarrow \gamma C + \delta D \tag{1-1}$$

$$\Delta_r G^\theta = \gamma \Delta_f G_C^\theta + \delta \Delta_f G_D^\theta - \alpha \Delta_f G_A^\theta - \beta \Delta_f G_B^\theta \tag{1-2}$$

When the system reacts, the reduction of the system's Gibbs free energy is equal to the maximum non-expansion externally work. For the battery system, the non-expansion work is only electrical work, which can be expressed by the Nernst equation:

$$\Delta_r G^\theta = -nEF \tag{1-3}$$

Where n is the number of electrons transferred by the electrode in the redox reaction, E is the thermodynamic balance voltage or electromotive force, and F is the Faraday constant (9.65×10^4 C/mol).

The energy density of battery is generally mass energy density with unit of Wh/kg or volume energy density with unit of Wh/L. The mass energy density and volume energy density can be expressed as below:

$$\varepsilon_M = \Delta_r G^\theta / \Sigma M; \varepsilon_V = \Delta_r G^\theta / \Sigma V \tag{1-4}$$

In which ΣM is the total molar mass of the reaction products and ΣV is the total molar volume of the reaction products.

For a certain electrode material, the theoretical capacity is:

$$\mathrm{C}_0 = nF/3.6M \ (unit\text{: mAh/g}) \tag{1-5}$$

Where M is the molar mass of the active material, n is the number of electrons gained and lost in the reaction and F is the Faraday constant.

According to **Formula 1-4**, the theoretical energy density and the theoretical voltage can be calculated based o the Gibbs free energy of the reactants and products when an electrochemical reaction is determined. The Gibbs free energy value can be found in the thermodynamics handbook[11-13].

Indicating the battery capacity or specific energy, the amount of discharge current should be given. In order to facilitate the comparison of different materials, it is usually expressed by C-rate (unit: C). C-rate refers to the current through the battery divided by its maximum capacity[14], and its value equals to the multiple of the rated capacity. For example, the 2C discharge means the discharge current will discharge the battery in 2 hours. For a battery with capacity of 100Ah, the discharge current is 6A.

The relationship between discharge current (I), capacity (C) and discharge time (t) is:

$$I = C/t \tag{1-6}$$

Besides the specific capacity and specific energy of the battery, the performance of LIB also includes cycle life and power. The main factor affecting the cycle life of LIB are[15]: (1) the volume expansion of active materials during charge and discharge, resulting in poor contact between the particles and the current collector; (2) corrosion of the electrode material; (3) internal short circuit of the battery; (4) electrolytic decomposition; (5) damage of the separator.

The power of the battery refers to the energy output per unit time with unit of W or kW. The specific power is the power output per unit mass or unit volume. The power indicates the operating current that the battery can withstand.

The theoretical power of a battery is calculated as below:

$$P = \frac{W}{t} = \frac{CE}{t} = \frac{ItE}{t} = IE \quad (1\text{-}7)$$

1.2.3 The factors influencing lithium-ion battery performance

With the wide application of LIBs including smart phones and electric vehicles, higher requirements are expected on the performance of LIBs, such as higher power density and rapid charge and discharge abilities. Therefore, the development of high-power LIB materials has become one of the focuses in research fields of LIBs.

The output power of LIB can be calculated as below formulas:

$$\mathrm{P}_{max} = \mathrm{I}_{max}\mathrm{V}_{max} \quad (1\text{-}8)$$

$$\mathrm{V}_{max} = \mathrm{U}_{oc} - \eta\mathrm{I}_{max} \quad (1\text{-}9)$$

$$\mathrm{U}_{oc} = \Delta\mathrm{E}/\mathrm{e} \quad (1\text{-}10)[16]$$

Where ΔE is the energy gap between the valence and conduction band of cathode and anode materials, U_{oc} is the open circuit voltage and η is the overpotential. In order to lower η, the electrode should be a good electron and ion conductor, and the mass transfer resistance at the interface of electrode and electrolyte should be small. In order to obtain a high current, the electrode-electrolyte interface must be large, which means the specific surface area of the active material must be large.

In summary, the power density of the electrode material is mainly affected by lithium ion diffusion rate, electron conductivity, and specific surface area of the material. At present, the methods to improve the power density of the materials and the rate performance mainly include: (1) preparation of nano-structured materials[17-19]; (2) coating with carbon[20-22]; (3) electrode structure design[23,24].

The difference of the size of the material will cause the difference in its electronic structure, which will cause huge changes in electrical, optical, thermal, and chemical properties. The design of nanostructures provides a new idea for optimizing the rate performance of LIB electrode materials. When nanomaterials are used in lithium-ion batteries, they have advantages of large specific surface area, short distance of lithium ion distance, small electrode polarization and good rate performance[17-19].

1.2.4 Mechanism of energy storage in Lithium ion battery

As the Figure 1.5 shown[25] , there are eight energy storage mechanisms for LIB, which are intercalation reaction, phase transition, conversion reaction, reversible chemical bonding, surface charging, free radical mechanism, under potential deposition and interfacial charging. The most common mechanisms in LIB are intercalation and phase transition.

1.2.4.1 Intercalation reaction

The material in which the intercalation mechanism occurs is usually a layered material, which can provide lithium ions or the material itself can provide vacancies for lithium ion storage. During the

charge and discharge processes, lithium ions are intercalated and deintercalated between the layers of the layered-structure material, which generally only causes a change of the spacing, and the lattice structure remains. Therefore, the electrode material of the intercalation reaction has an excellent cycle life. The specific capacity of the electrode material of the intercalation mechanism is determined by the number of moles of lithium ions that can be intercalated into the material.

1.2.4.2 Phase transition

During the reaction, there is phase transition occurs in the charge and discharge. For instance, $LiFePO_4$ is converted to $FePO_4$ during charging[26], and $Li_4Ti_5O_{12}$ is changed to $Li_7Ti_5O_{12}$ during discharging[27]. For phase transition electrode materials, there will be a corresponding voltage plateau on the charge and discharge curve when phase transition occurs. Since the Gibbs free energy of the electrochemical reaction does not change during the two-phase transition as well as the intercalation and deintercalation of the lithium ions, the corresponding voltage does not change and a voltage plateau is generated.

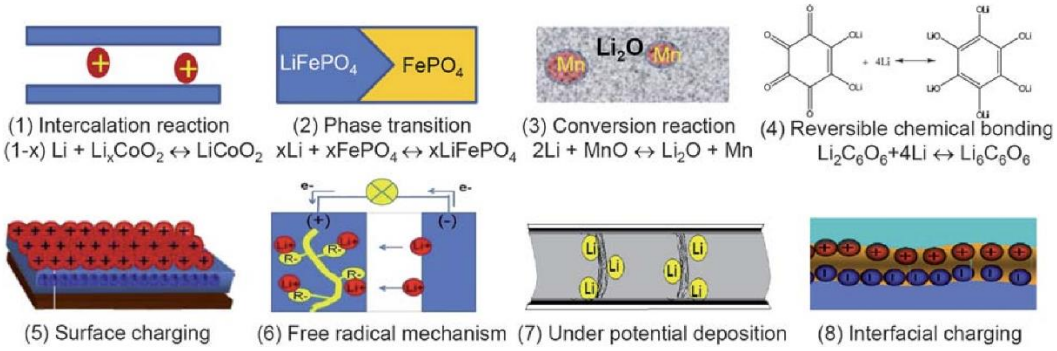

Figure 1.5 Scheme of reversible lithium storage mechanisms.[25]

1.3 Materials for anode

The research and development of anode materials for LIBs have gone through several generations. The first-generation negative electrode materials directly uses lithium metal with high capacity (3860mAh/g), but there might be safety problem of short circuit caused by the lithium dendrites during charge and discharge[4]. The second generation of lithium alloy solves the lithium dendrites problems, however, the lithium alloy would expand during charge and discharge process due to the size mismatch of the vacancies in crystal and lithium ions with a result of crystal structure collapsing[28]. The third-generation anode material is graphite anode developed on the theoretical basis of rocking-chair batteries[5,6]. Because the potential of the graphene is close to that of lithium, the graphite with a layered structure is beneficial to the intercalation and deintercalation of lithium, which significantly improves the cycle life and safety performance.

Although there are various types of anode materials are studied currently, there are few materials with commercial prospects. With the application requirements for high power density and high energy density of LIBs, the focus of research is on a new generation of anode materials with high specific capacity and long cycle life.

1.3.1 Titanium dioxide nanosheets

At present, the μ_A of most of the anode materials is higher than the LUMO of the electrolyte, which will have a reduction reaction with the electrolyte to form a non-conducting passivation film. They have a potential close to that of lithium metal, lithium metal will deposit on the surface of the anode during high current charging and discharging, posing safety hazards. Titanium dioxide(TiO_2) has a theoretical capacity of 170 mAh/g, which is lower than that of graphite[29]. The working voltage of TiO_2 is higher(~1.7V vs. Li/Li^+) than graphite anode materials (~0.5V vs. Li/Li^+), and the battery system is safer. Moreover, TiO_2 has a small volume change and a stable lattice structure. Therefore, TiO_2 has been paid more and more attention as an electrode. The open crystal structure and the electronic structure of Ti ions allow TiO_2 to accept electrons from foreign ions and provide vacancies for intercalated cations(Li^+, H^+ and Na^+ etc.).

Although TiO_2 has good application prospects, its relatively poor conductivity and wide band gap limit its application in energy storage and conversion. A strategy of nanostructure engineering can improve the specific surface area of the titanium dioxide, increasing the contact area between the electrolyte and the electrode material, reducing the lithium ion diffusion, and increasing the specific capacitance. Due to the advantages, the application of nano-scale TiO_2 nanosheets were studied by researchers all over the world[30,31]. Liu et al.[32] used ionic liquids containing lithium salts as reaction additives to prepare a "sandwich"-like structure, which is stacked by ultra-thin titanium dioxide nanosheets. The ultra-thin nanosheet structure can shorten the lithium ion in the crystal. The internal diffusion path and the pore structure between the nanosheets were conducive to the rapid penetration of the electrolyte, so it had excellent rate and cycle performance. When charging and discharging at 50C (charging for 1.2min), the specific capacity of 109mAh/g could be obtained, and it hardly decayed after 150 cycles.

1.3.2 Nb-based materials

Currently, many Nb-based materials such as Nb_2O_5 and $TiNb_2O_7$ exhibit excellent electrochemical performance as negative electrode materials and have been extensively studied.

Nb_2O_5 is an intercalated material with multiple redox couples(Nb^{5+}/Nb^{4+}, Nb^{4+}/Nb^{3+}) and low volume expansion. These properties make it have high safety and good structural stability when used as a anode material for LIBs. The reversible lithium ion intercalation and deintercalation reactions in Nb_2O_5 are as follows:

$$Nb_2O_5 + xLi^+ + xe^- \leftrightarrow Li_xNb_2O_5 \quad (1\text{-}11)$$

Where x is the stoichiometric number of intercalation/deintercalation of lithium ions.

The intercalation reaction of niobium oxide is very sensitive to the preparation temperature and particle size. Nb_2O_5 has many crystal forms at different calcination temperatures, such as orthorhombic (O-Nb_2O_5), pseudohexagonal (TT-Nb_2O_5), tetragonal (T-Nb_2O_5), monoclinic (M-Nb_2O_5) structures[33,34]. Previous study has found that 2D layer structure of T-Nb_2O_5 has the most excellent electrochemical performance with longer cycle life and more favorable for reversible Li^+ intercalation[35]. However, due to poor electronic conductivity and ion diffusion ability, its rate performance still needs to be further improved.

In addition to Nb and O elements, some niobium oxides also contain another metal element to form $M_xNb_yO_z$ (M=Ti, Sn, W, Ba, Bi, Cr, Li. V, K, P, Pb etc.). Such compounds are called niobium-based

composite oxides[36]. The metal atom enhances electronic conductivity and stability of the crystal structure, and the capacity of the electrode can be increased as well due to the participation of multivalent M atoms, such as Ti[37].

$TiNb_2O_7$ is a monoclinic crystal, with Wadsley-Roth phase. The shear plane structure in the crystal prohibits Li^+ diffusion perpendicular to the channel, which can keep the frame open and provide a stable structure. The ion and electron conduction has strong anisotropy, and it can be approximated as one-dimensional along the channel direction (b-axis). The octahedral ReO_3-like block in $TiNb_2O_7$ makes lithium diffusion easier, and the barrier is <100meV while it also has a larger Li^+ ion diffusion coefficient. However, when Na^+, K^+ and Mg^{2+} are deintercalated, the diffusion barriers are higher, which means this structure is more suitable for Li^+ intercalation[38]. Wang et al.[39] used tetrabutyl titanate and niobium chloride to synthesize Ti-Nb oxide composite microspheres. The synergistic effect of the multi-phase overcome the problem of low conductivity of traditional oxides, thus promoting the electrochemical cycle stability of the composite anode material. In the meantime, the special graded mesopores could effectively shorten the Li^+ diffusion distance and provide interconnected channels for fast electron transmission. Guo et al.[40] used niobium ethoxide and tetrabutyl titanate as precursors to prepare high performance $TiNb_2O_7$ materials with interconnected nanoporous frameworks composed of nanocrystals. The material exhibited a reversible storage capacity of up to 281 mAh/g, higher rate performance and longer cycle life. And the capacity retention rate was still 84% after one thousand cycles. Yu et al.[41] improved the electrochemical performance of $TiNb_{24}O_{62}$ nanowires by nitrogen-doped carbon coating, and found that their electronic conductivity and electrochemical activity were greatly improved.

1.3.3 $TiNbO_5$ and Ti_5NbO_{14} nanosheets as anode materials

Nanomaterials can be categorized into 0D nanomaterials (nanoparticles), 1D nanomaterials (nanotubes, nanorods, and nanowires), 2D nanomaterials (nanosheets) and 3D nanomaterials (nanonetwork). Due to the large specific surface area and the excellent performance of lithium storage of nanomaterials, more studies were carried on nanomaterials as electrode materials in supercapacitors, lithium and sodium ion batteries.

$TiNbO_5$ nanosheets have been confirmed by Shen et al. that it is a good candidate for sodium storage[42]. The annealed $Ti_2Nb_2O_9$ nanosheets exhibited a capacity of 250 mAh/g at 50 mA/g at a suitable average voltage of ~0.7V. Osada et al.[43] produced multilayered $TiNbO_5$, Ti_2NbO_7, Ti_5NbO_{14} nanosheets by Langmuir-Blodgett (LB) process for high-κ nanodielectrics. The octahedral distortion caused by Nb incorporation led to a giant molecular polarizability, which exhibited a high dielectric constant.

1.4 The objective and main content of this research

Due to higher requirements for the performance of LIBs, the traditional titanium dioxide cannot meet the requirements. Therefore, there is an urgent need to prepare novel electrode materials with larger reversible specific capacity and better cycle and rate performance. Based on the previous studies, TiNbO nanosheets were used as anode materials in sodium storage and high dielectrics.

In this research, exfoliation process was performed to fabricate two different TiNbO nanosheets and bulk materials of $TiNbO_5$ and Ti_5NbO_{14} with different ratio of Ti and Nb respectively for comparison as high rate electrodes for LIBs. And the conditions of exfoliation and protonation processes were optimized for Ti_5NbO_{14} nanosheets. Langmuir-Blodgett (LB) process as well as Atomic force

microscopy (AFM) were taken place to investigate the efficiency of the production of nanosheets. The four electrode materials were characterized by X-ray diffraction (XRD) and Scanning electron microscopy (SEM). The electrochemical measurements including rate charge-discharge test, cyclic voltammetry (CV), Electrochemical impedance spectroscopy (EIS) and long cycling test were performed for every material. The influence of Ti:Nb ratio and difference between nanosheet and bulk materials were discussed and explained.

2 Experimental

2.1 Experimental reagents

The experimental reagents used in the experiments are shown as below **Table 2.1**:

Chemical	Abbreviation	CAS-No.	Purity	Supplier
Potassium carbonate	K_2CO_3	584-08-7	≥99%	Sigma Aldrich
Titanium(IV) dioxide, anatase	TiO_2	13463-67-7	≥99%	Sigma Aldrich
Niobium(V) oxide	Nb_2O_5	1313-96-8	99.9%	Sigma Aldrich
Tetrabutylammonium hydroxide	TBAOH	2052-49-5	40wt% in H_2O	Sigma Aldrich
Hydrochloric acid	HCl	7647-01-0	37% in H_2O	Sigma Aldrich
Nitric acid	HNO_3	7697-37-2	65% in H_2O	Acros Organics
1-Methyl-2-pyrrolidinone	NMP	872-50-4	≥99%	Sigma Aldrich
Poly(vinylidene fluoride)	PVDF	24937-79-9	M_w~534000	Sigma Aldrich
Carbon black	C	1333-86-4	≥99%	Super P

Table 2.1 Experiment reagents used in experiments

2.2 Experimental instruments

The experimental instruments used in the experiments are listed as below **Table 2.1**:

Instrument	Supplier and Model
Centrifuge	Thermo Scientific Biofuge Primo
Balance	Mettler Toledo
Muffle furnace	Vecstar
LayerBuilder	KSV
Electrochemistry workstation	Biologic VMP-300
Battery testing system	Neware
X-ray diffraction	PANalytical X'Pert Pro
Atomic force microscopy	Veeco
Scanning electron microscopy	Zeiss Merlin

Table 2.2 Experiment instruments used in experiments

2.3 Experimental methods

2.3.1 Fabrication of TiNbO nanosheets

The synthesis of TiNbO nanosheets took the previous study[42] as reference and was optimized in this project. It started from the preparation of $KTiNbO_5$ and $K_3Ti_5NbO_{14}$ powder by solid state reaction. First, the powders of K_2CO_3, TiO_2 and Nb_2O_5 in two molar ratios (1:2:1 and 3:10:1) were mixed and ground for 10-15 min, and then mixed on a roller bench for 24 hours. The mixture was calcined at 1100℃ for 10 hours in a platinum crucible. After that, the calcined KTiNbO powder was protonated by mixing 2g KTiNbO, 40mL HNO_3 (65wt% in H_2O) and 240mL deionized water. The pronation process was performed for 4 days, where the acid solution was renewed after 48 hours by standing still the solution and pouring out the upper solution. The protonated HTiNbO powder was then vacuum filtered and washed 3 times by water. Finally, the washed powder was dried in air at room temperature overnight. The protonation process weakened the Coulombic interactions between the

nanosheet layers. The synthesized HTiNbO was used as bulk electrode materials and exfoliation for nanosheets.

The exfoliation was conducted by adding 0.44g $HTiNbO_5$ powder and 1.9mL TBAOH (40wt% in H_2O) in a molar ratio of 1:1.5 in 150mL DI water. The stirring speed was set up to 250 rpm and last for 3 days. The exfoliation process of $H_3Ti_5NbO_{14}$ was explored with the length and concentration of the process, and characterized by LB and AFM. After the reaction, the solution was centrifuged at 2000 rpm for 5 minutes to get the upper solution which could filter the particles which have not been exfoliated successfully. The upper solution was then centrifuged at 8000 rpm for 20 min to concentrate the nanosheet solution in ~20mL DI water. By using 2-3 mL 2 M HCl solution, the nanosheets were precipitated and washed by water for 3 times. After that, the nanosheets were centrifuged at 8000 rpm for 3 minutes. Finally, the nanosheets were frozen for 24 hours and then dried in vacuum oven at room temperature. **Figure 2.1** shows the scheme of the process.

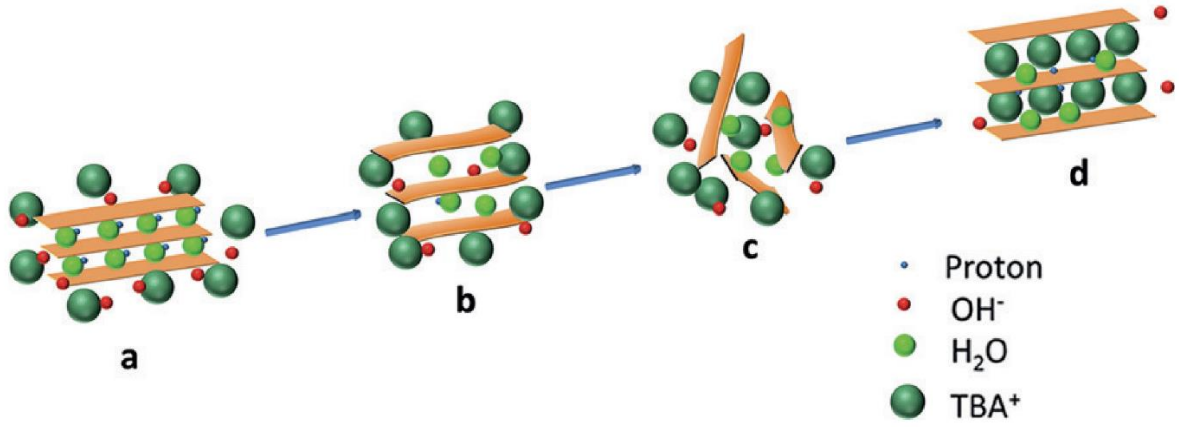

Figure 2.1 Schematic of the exfoliation process. [44]

2.3.2 Langmuir-Blodgett deposition

The LB deposition in this project was to examine the efficiency of the exfoliation process. It needs a hydrophilic/hydrophobic substrate, a solution of nanosheets and a LB deposition set-up.

The preparation procedure is described as below: Firstly, 5 mL sample solution taken from the reaction solution directly was diluted into 180 mL H_2O to concentrate nanosheets at liquid-gas interface. 50 mL of the diluted nanosheets solution was carefully filled into a Teflon LB trough which washed by ethanol and blew by nitrogen. The LB trough was made up by hydrophobic plastics in order to avoid the nanosheets stick on the surface of the set-up. Secondly, a 5mm ×5mm Si wafer was immersed in acetone for 10 minutes, and oxygen plasma was applied to the Si substrate for 15 minutes to form a layer of incompletely oxidized silicon oxide. The substrate was then stuck on a glass flake for LB deposition and loaded in the trough of the LB set-up. Finally, stabilize the solution in the trough for 15 minutes.

The whole deposition process can be divided into two steps. In the first step, there were two plastic barriers moving along the interface to compress the nanosheets and form a monolayer of nanosheets at the liquid-gas interface while the surface pressure was increasing. When the surface pressure met a plateau, which was a sign that a largely covered monolayer of nanosheets were generated. The

second step started with the surface pressure plateau, the substrate was slowly lift up from the solution and the barriers moved along the interface to keep the surface pressure as a constant with the one at the lift up point. In this project, the LB deposition was applied to examine the yield of exfoliation. If the yield was high enough, the surface pressure plateau would reached the plateau and the substrate was fully covered by nanosheets. After the deposition, the substrate was heat up at 400℃ for 30 minutes and ready for AFM characterization.

2.3.3 Electrochemical characterization

The working electrode was made up of the electrode material (both nanosheets and bulks), Super P carbon black and PVDF in a mass ratio of active material: conductive agent: binder = 5:4:1. 10 mg nanosheets/bulks and 8 mg carbon black were mixed and ground for 20 minutes, and then the mixture was added into 40 μL 1g/20mL PVDF/NMP solution and 80 μL NMP. After that, it was put in a ultrasonic cleaner for 60 minutes to mix them homogeneously. The sample bottle was shaken every 20 minutes. The mixture was spread uniformly on the surface of a copper foil and heat on a hot plate at 65℃ until the NMP was evaporated. Finally, the electrode was dried in a vacuum oven at 60℃ for 12 h.

The batteries were assembled in a argon atmosphere glove box with working electrode described as above, Na metal as the counter electrode and reference electrode, glass fiber separator and 1 M $LiPF_6$ in 1:1 ethylene carbonate dimethyl carbonate (EC: DMC) as electrolyte. The assembled batteries were characterized in Biologic VMP-300 electrochemistry workstation with cyclic voltammetry (CV), galvanostatic rate charge/discharge experiments between 1 V to 3 V. EIS were performed at steady-state after resting from the galvanostatic rate charge/discharge experiments. Long cycling test was performed on Neware battery testing system from 1 V to 3 V.

2.3.4 Materials characterization

The X-ray diffraction for all the powder and nanosheets was done on a PANalytical X'Pert Pro with a Cu Kα (λ = 1.54178) filter scanning from 5° to 70° to confirm the synthesis of the target product.

Atomic force microscopy for Ti_5NbO_{14} nanosheets was done by a Veeco Dimension Icon in tapping mode on a Si substrate, and the results were analyzed by Gwyddion version 2.58 software.

High resolution scanning electron microscopy was performed on Zeiss MERLIN to observe the morphology of the particles.

3 Results and Discussion

In this chapter, I will discuss the optimization of the exfoliation progress and the all characterization result.

3.1 Characterization of precursors

Since all the precursors including $KTiNbO_5$, $HTiNbO_5$, $K_3Ti_5NbO_{14}$ and $H_3Ti_5NbO_{14}$ are all white powders. It is essential to characterize all the precursors by XRD to confirm the successful synthesis of these layered structure powders. Besides the XRD characterization, SEM was performed to observe the morphology. Since the performance of the electrodes strongly depends on the size of the particle and nanosheets. The morphology information was required necessarily.

3.1.1 Scanning electron microscopy

SEM shows the clear results that bulk $HTiNbO_5$ had layered structures in 100 Kx magnification (**Figure 3.1c**) and it can be seen that the particles were irregular in sizes, ranging from 1 μm to 20 μm.

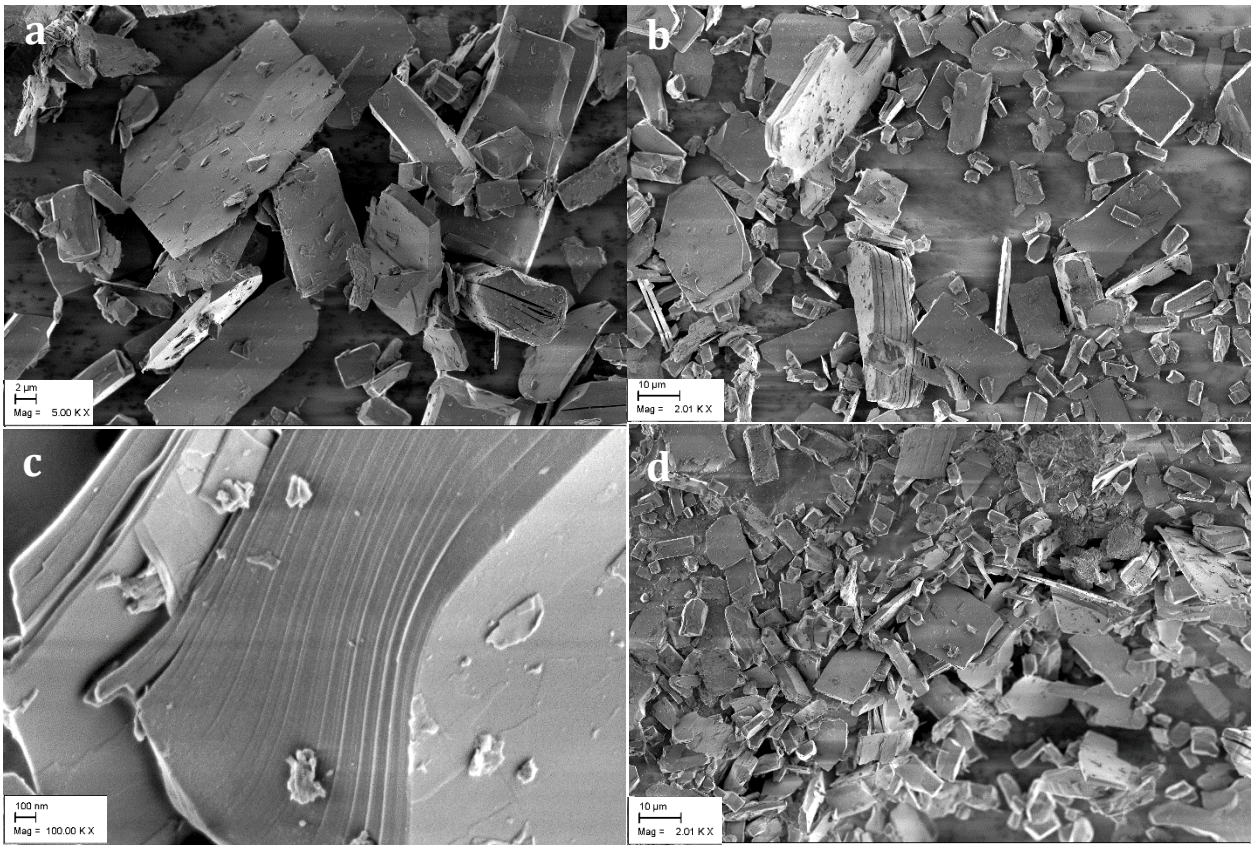

Figure 3.1 SEM images of bulk $HTiNbO_5$ particles in low (b)(d), medium (a) and high (c) magnifications.

The bulk $K_3Ti_5NbO_{14}$ (**Figure 3.2a, c, e**) and $H_3Ti_5NbO_{14}$ (**Figure 3.2b, d, f**) have similar layered structure which can be observed in high magnification images. These layered structures of the precursors present that it is possible to synthesize the nanosheets by exfoliation. The size of bulk

$K_3Ti_5NbO_{14}$ is approximately 2 μm while irregular needle-like and flake-like structures appear in the grains of $H_3Ti_5NbO_{14}$.

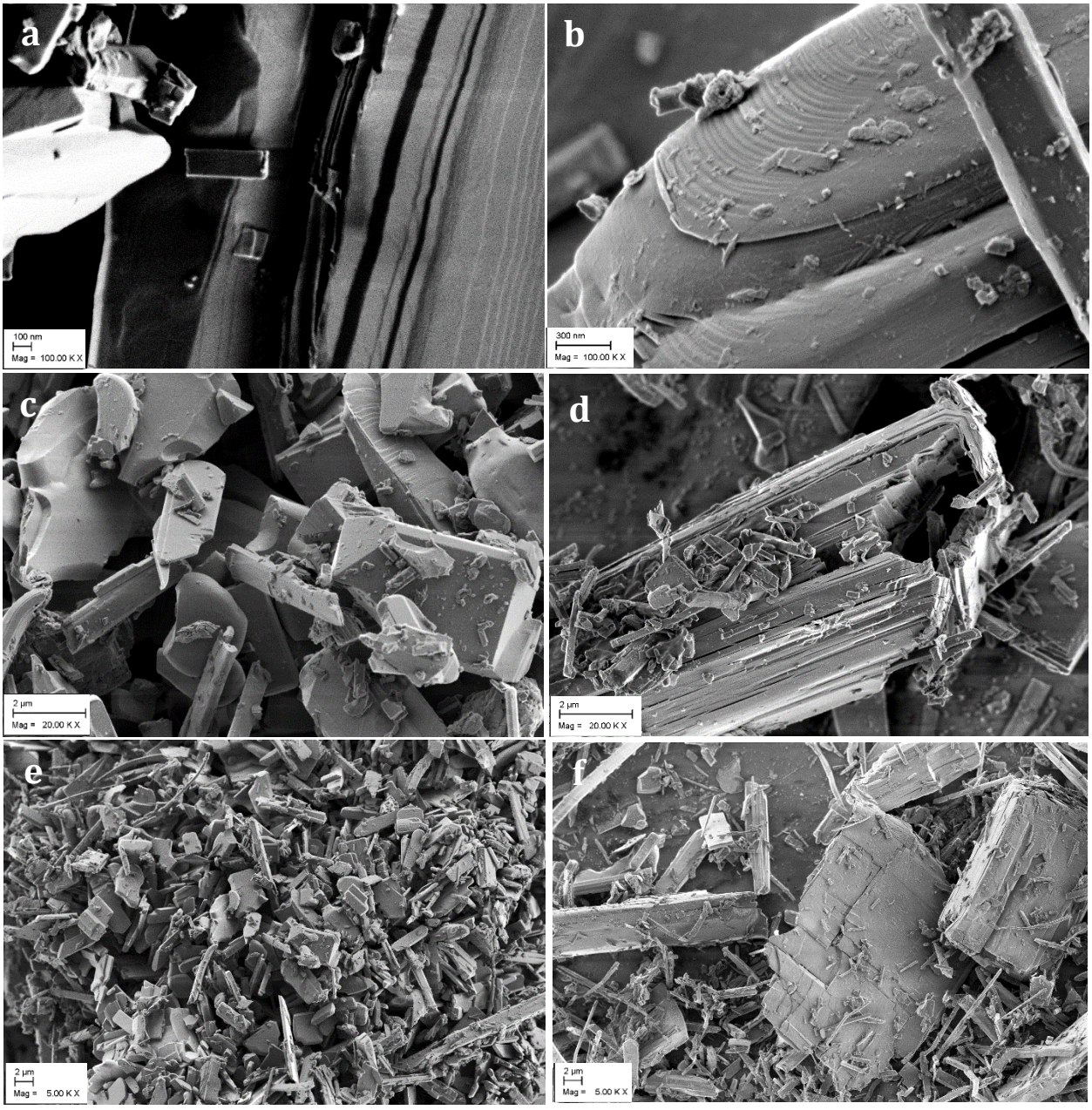

Figure 3.2 SEM images of bulk $K_3Ti_5NbO_{14}$ in high (a), medium (c) and low (e) magnifications and $H_3Ti_5NbO_{14}$ in high (b), medium (d) and low (f) magnifications.

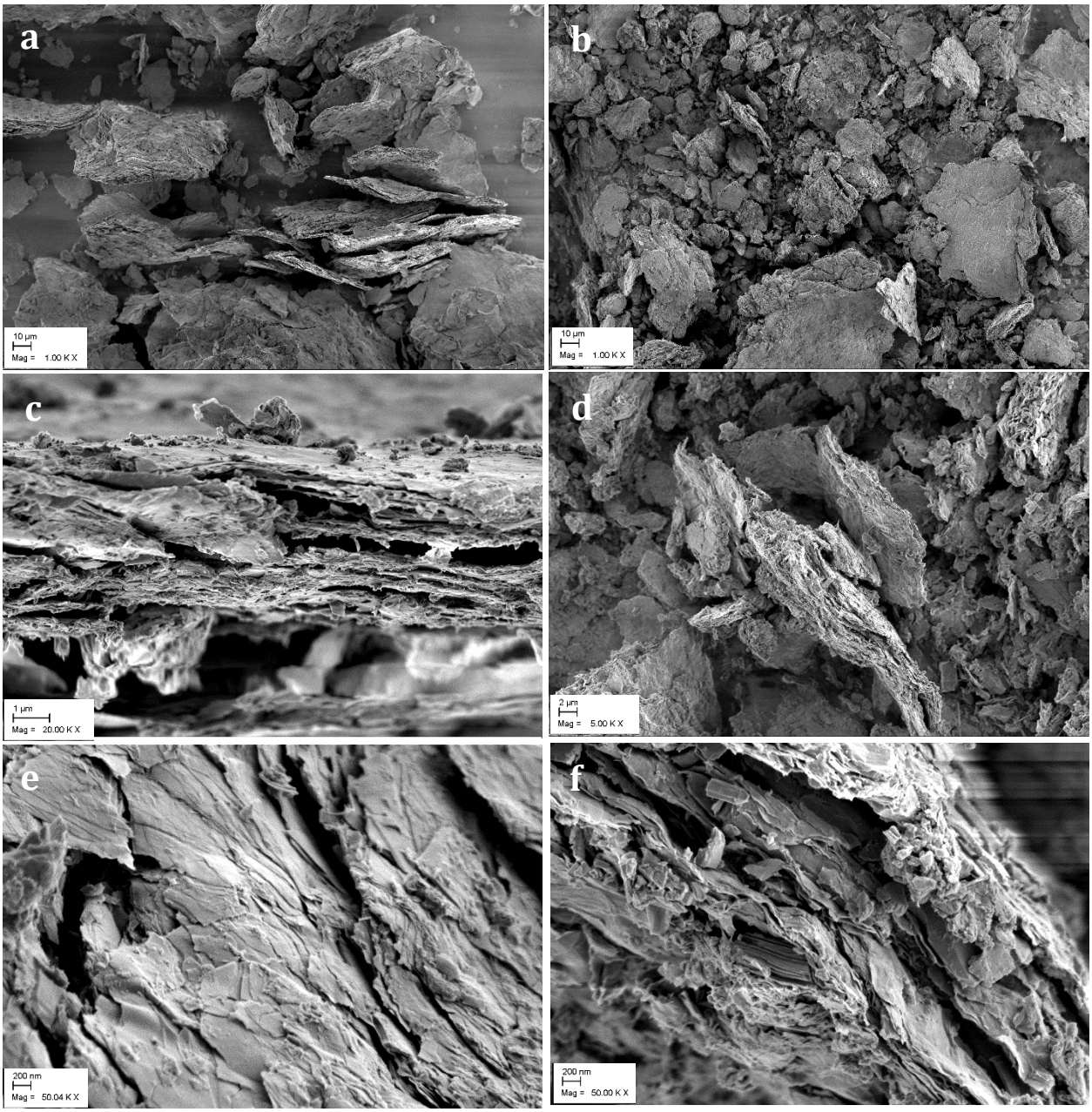

Figure 3.3 SEM images of Ti_5NbO_{14} nanosheets in high (a), medium (c) and low (e) magnifications and Ti_5NbO_{14} nanosheets in high (b), medium (d) and low (f) magnifications

It can be observed that the exfoliated nanosheets have different morphology versus the bulk ones. The fluffy structures in the nanosheets indicate that the surface area of the nanosheets was larger. Clear layered structure is shown in the cross-sectional **Figure 3.3c**. Since the nanosheets were obtained by using H^+ to remove the extra TBAOH, some of the nanosheets were restacked under the acidic condition, therefore we cannot observe the monolayer in SEM images.

3.1.2 X-ray diffraction

XRD test can specifically characterize the phase characteristics of all the precursors. In **Figure 3.4a**, the XRD results of $KTiNbO_5$ are matched with the reference $KTiNbO_5$ in HighScore Plus database. The obvious $KTiNbO_5$ characteristic peaks (ICSD 98-001-6557) can be observed, and the diffraction peaks at 2θ = 27.598°, 27.604°, 30.938°, 32.183° and 47.942° correspond to (200), (013), (113), (106) and (020) crystal planes of $KTiNbO_5$ respectively. In addition, the diffraction peaks at 60° to 80° are hard to be identified due to the dense peaks in the reference pattern.

After the protonation, the dried powder of $HTiNbO_5$ has been tested by XRD for the phase information as well (**Figure 3.4b**). The three highest peaks at 10.602°, 17.228° and 24.141° are matched with the reference (ICSD 98-003-1797) though the peaks located from 50° to 80° are barely identified. However the correspondence of the highest peaks can be considered as the success of protonation, and the total pattern could be indexed based on the same orthorhombic symmetry as the reference.

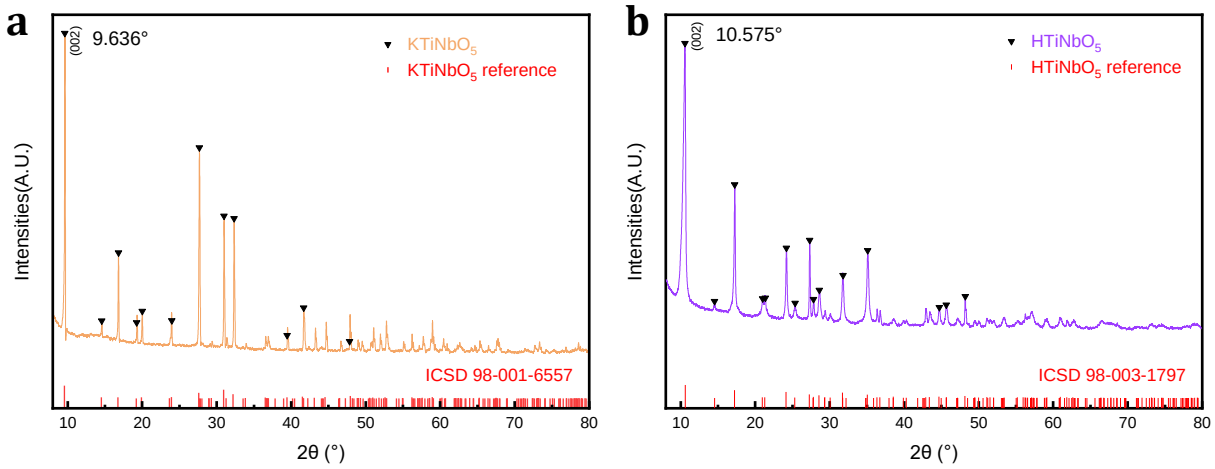

Figure 3.4 XRD patterns of (a) $KTiNbO_5$ and reference (ICSD 98-001-6557) and (b) $HTiNbO_5$ and reference (ICSD 98-003-1797).

The XRD test results of $K_3Ti_5NbO_{14}$ and $H_3Ti_5NbO_{14}$ were analyzed as same method above by comparing with reference in database. In the **Figure 3.5a**, the peak which has the highest intensities at 9.809° is matched with the reference ICSD 98-001-6374. However, there aree two unknown peaks at 11.57° and 11.94° which are not occur in the reference pattern. Based on the database in HighScore Plus, the two unknown peaks might belong to the KTi_3NbO_9 (ICSD 98-001-6558). Since there are several peaks cannot be addressed to the reference, there were some impurities such as oxides in other Ti:Nb ratio were produced at the solid-state synthesis.

Since the XRD information of $H_3Ti_5NbO_{14}$ is not included in the database, the results are compared with a reported paper[45]. According to **Figure 3.5b**, there is a slight shift of the first peak of the two powders from 9.89° to 10.06°, and a peak at 15.27° disappeares while a peak at 17.80° occurs after the protonation, which is demonstrated by the reported paper (**Figure A.5.1**). The first peak also indicates the d-spacing between the crystal layers, as the peak information, the $H_3Ti_5NbO_{14}$ has lower d-spacing than that of $K_3Ti_5NbO_{14}$. Due to the K atom has larger size than the H atom, it is reasonable that the $H_3Ti_5NbO_{14}$ has lower d-spacing. Although the two undefined peaks also occurs in the XRD

pattern of $H_3Ti_5NbO_{14}$, the shift of the peak and the newly-occurred peak are signs of fabrication of $H_3Ti_5NbO_{14}$.

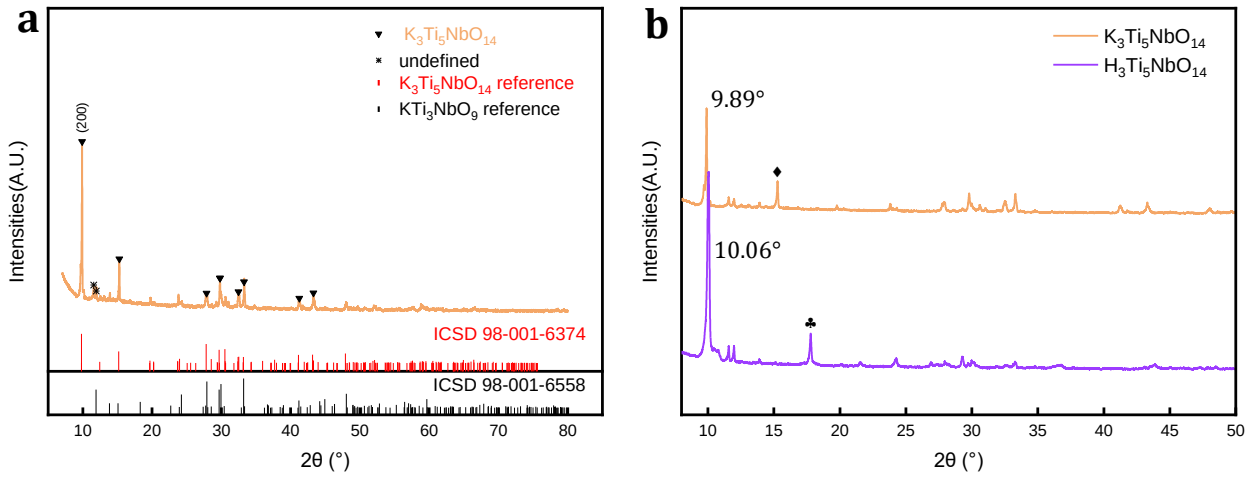

Figure 3.5 XRD patterns of (a) $K_3Ti_5NbO_{14}$, reference $K_3Ti_5NbO_{14}$ (ICSD 98-001-6374) and reference KTi_3NbO_9 (ICSD 98-001-6558) and (b) $H_3Ti_5NbO_{14}$.

Powder XRD were performed for $TiNbO_5$ nanosheets, while the film XRD were done for Ti_5NbO_{14} nanosheets on a Silicon due to the low signal of its powder. Since the low signals of the nanosheets, the only visible peak occurred in the low angle range. The peak occurs in this range represents the d-spacing of the layers of the nanosheets. Due to the Bragg's law:

$$d = \frac{n\lambda}{2sin\theta} \tag{2-1}$$

Where λ is the wavelength of the incident X-ray (1.5406Å), Θ is the peak position, n is the order of diffraction (=1) and d is the d-spacing. According to the peak positions of the nanosheets indicated in **Figure 3.6**, the d-spacing of the $TiNbO_5$ is 8.458Å while that of Ti_5NbO_{14} is 8.954Å.

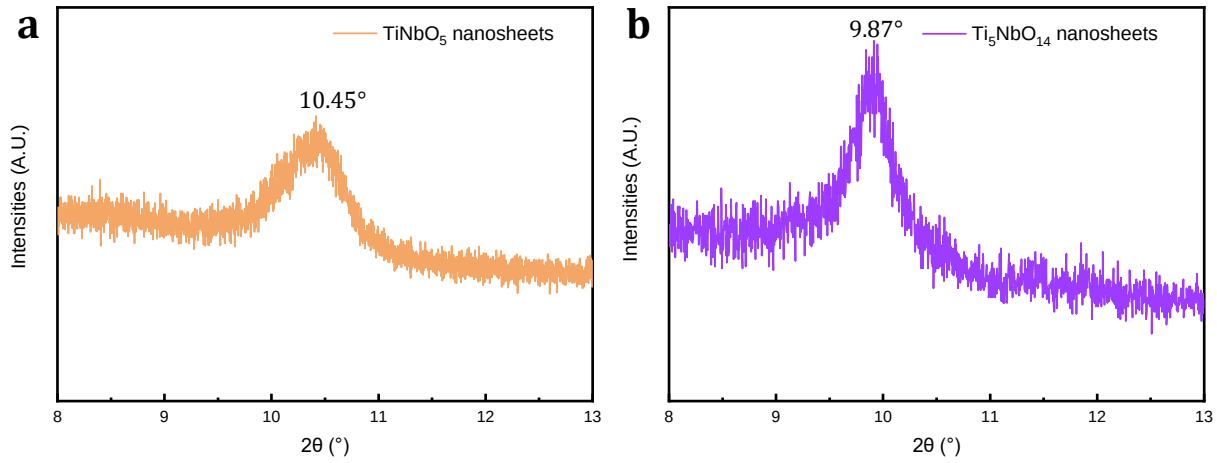

Figure 3.6 XRD patterns of (a) $TiNbO_5$ nanosheets and (b) Ti_5NbO_{14} nanosheets.

3.2 Synthesis optimization for $TiNbO_5$ nanosheets

In this study, the $TiNbO_5$ nanosheets were dried by two different methods. In the first method, the protonated powder was dried in vacuum oven at 60°C and the exfoliated nanosheets was centrifuged and calcined in a Muffle furnace at 450°C for 10 hours so that the powder we obtained was TBA^+ with $TiNbO_5^-$, while in the second one, the protonated powder was dried in air at room temperature, and HCl was added into the suspension of the nanosheets and then they were frozen and dried in vacuum oven at room temperature. The electrodes fabricated by these two methods were compared by rate charge-discharge electrochemical characterization in a ratio of active material: conductive agent: binder = 7:2:1. Less amount of Super P carbon black was used in this optimization to exclude the influence of the conductive agent. The results are compared as below in **Figure 3.7**:

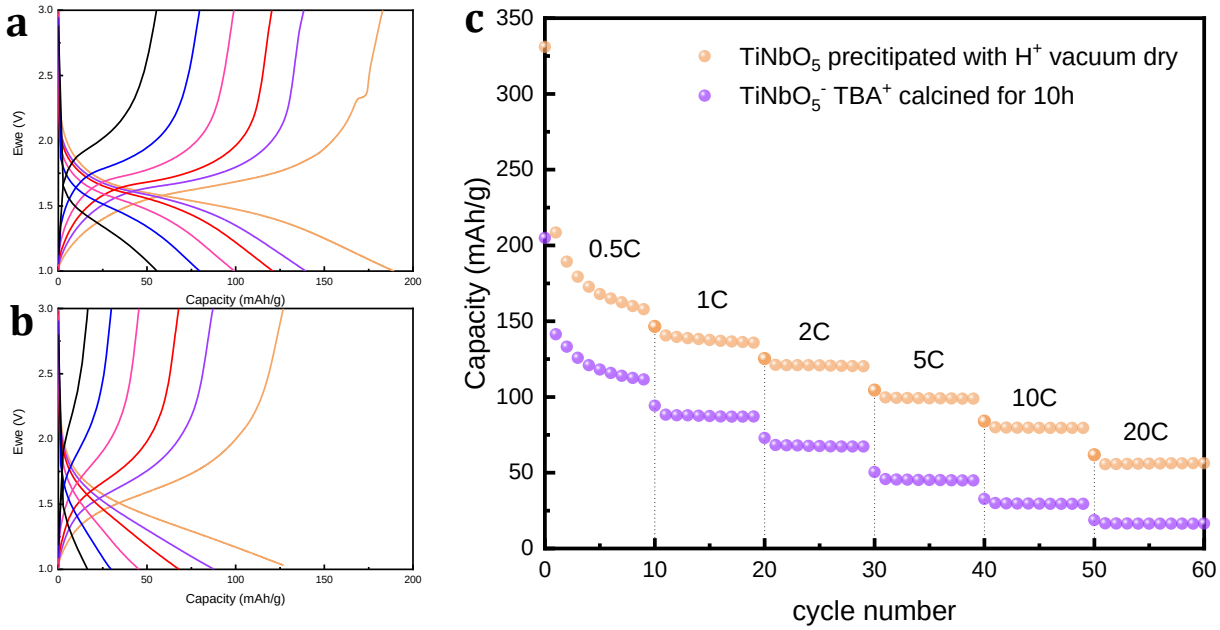

Figure 3.7 Rate charge-discharge curves of electrodes made with (a) $TiNbO_5$nanosheets precipitated with H^+ and dried in vacuum oven at room temperature and (b) $TiNbO_5^-$ TBA^+ nanosheets calcined for 10h in 7:2:1 ratio. (c) Comparison of two nanosheets by capacity vs. cycle number.

Starting with a capacity over 150 mAh/g at 0.5C, the $TiNbO_5$ dried by vacuum oven has a higher capacity than the other one. The electrochemical performance of the calcined nanosheets TBA^+ is too poor to have only 16 mAh/g at the ending of the test for 20C. The significant difference can be observed obviously in **Figure 3.7c** by the comparison of the capacity versus cycle number plot of the both nanosheets.

The reason of the difference is not clear yet. But according to the different synthesis methods, we assumed that the reason is that the TBA^+ particles were intercalated between the layers of the nanosheets as **Figure 2.1d**, and due to the fast burn out of the TBAOH during the calcination, the layers were restacked together. And another factor is that the protonated powder was dried at 60°C, which makes the spacing between layers in the $HTiNbO_5$ crystal intends to decrease because of the quick evaporation of the H_2O between the crystal layers. Therefore the nanosheets synthesized by

the second method described above has higher electrochemical rate performance. As a result, all the nanosheets in this research were synthesized by the method described above.

3.3 Exfoliation optimization for Ti_5NbO_{14} nanosheets

The exfoliation time and volume of the reaction solution during the exfoliation was explored. The exfoliation condition for the $TiNbO_5$ was confirmed by a member in IMS group that the condition of the exfoliation of nanosheets was mixing 0.44g $HTiNbO_5$ powder and 1.9mL TBAOH (40wt% in H_2O) in a molar ratio of 1:1.5 in 150mL DI water for 3 days. However, due to the different structure and atomic force between the layers of the crystal, the condition of the exfoliation for Ti_5NbO_{14} nanosheets was unclear yet. Therefore, in this project, the condition of the exfoliation for Ti_5NbO_{14} was examined by LB process and AFM to test the coverage of nanosheets on a Silicon substrate.

The set-up of the exfoliation is listed as **Table 3.1**:

No.	$m_{H_3Ti_5NbO_{14}}$ (g)	V_{TBAOH}(mL)	V_{H_2O}(mL)	Time(h)
1	0.4	2.11	150	24
2	0.4	2.11	150	72
3	0.4	2.11	150	96
4	0.2	1.055	40	17.5
5	0.2	1.055	40	23
6	0.2	1.055	40	29.5

Table 3.1 Series of exfoliation conditions for Ti_5NbO_{14} nanosheets.

At first, the 5:1 oxide nanosheets were exfoliation under the same condition as the 1:1 ones for three days. However the coverage of the nanosheets were only around 80%. There were two possible reasons: (1) the exfoliation time was not long enough so that the concentration of nanosheets were not high enough to cover the substrate fully; (2) the exfoliation time was too long that the nanosheets were restacked but only the monolayer nanosheets could be covered on Silicon by LB deposition. Therefore, the Ti_5NbO_{14} were exfoliated for one and four days respectively, and tested by same method and the AFM images for the set-up 1-3 were shown in **Figure 3.8**.

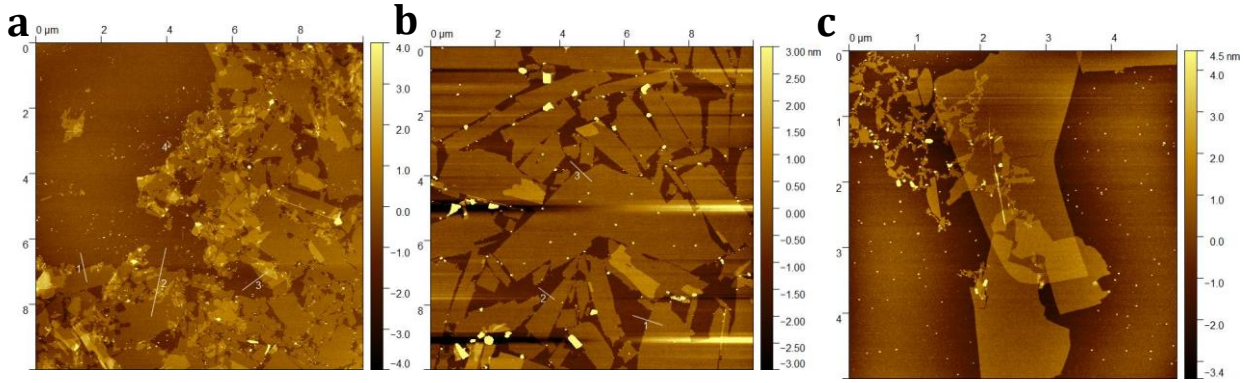

Figure 3.8 AFM images of exfoliated Ti_5NbO_{14} for (a) 1 days, (b) 3day and (c) 4 days.

According to the AFM results in **Figure 3.8**, the nanosheets produced with the same method as TiNbO5 had >80% coverage, while those exfoliated for only one day had a coverage ~75%. The four-day exfoliation product had only 30% coverage, which represents that 96-hour exfoliation was too long so that the nanosheets were restacked again.

Due to the exfoliation results cannot provide full coverage for nanosheets on Silicon substrate, I decide to change the volume of the water into the reaction so that the pH of the reaction system as well as the concentration of the TNAOH could be increased to accelerate the reaction. The recipe of the new set-ups was provided in **Table 3.1** as No. 4-6. Although none of them reached a plateau during the LB deposition, set-up 4-6 reached high surface pressures as 7.5, 15 and 19 mN/m respectively. And their AFM characterization was shown as **Figure 3.9**.

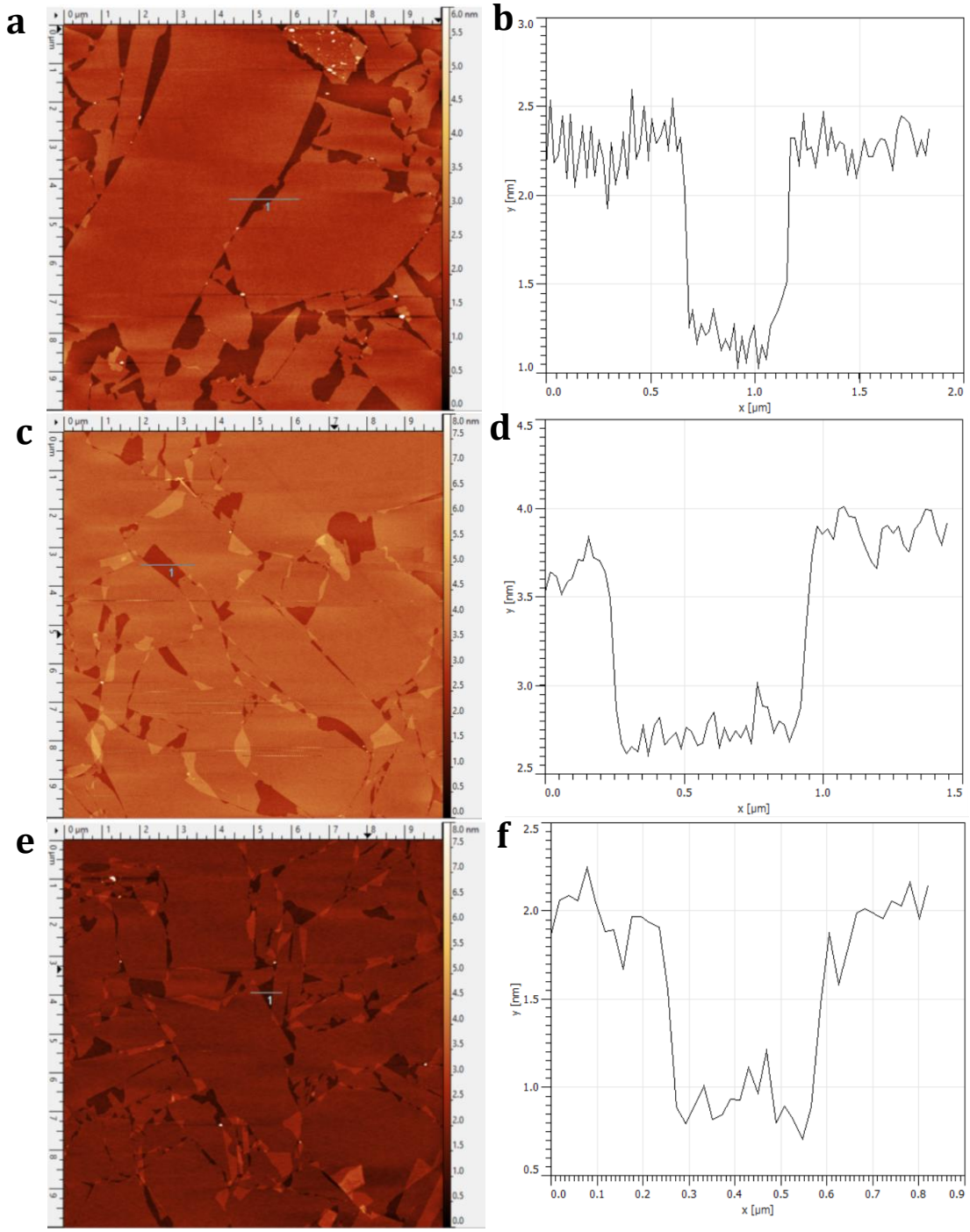

Figure 3.9 AFM images (a,c,e) and height measurements (b,d,f) of sample 4-6 respectively.

For the AFM result for sample 4, the coverage was approximately 90%, while those for sample 5 and sample 6 were higher than 95%. And there were some overlapped area in the them. In addition, the height measurements indicate that the average thickness of the Ti_5NbO_{14} was ~1nm.

In conclusion, the set-ups of sample 5 & 6 were proper exfoliation conditions. In the experiments, we mixed 0.4g $H_3Ti_5NbO_{14}$, 2.11 mL TBAOH and 80 mL DI water to react for 24 hours, which doubled the dosage of set-up 5.

3.4 Electrochemical characterization

In this section, all test results of the electrochemical characterization were provided and discussed, including rate charge-discharge test, difference scan rate CV, EIS and long cycle life test. And the results will be compared between same Ti:Nb ratio bulk and nanosheets, different ratio bulk and nanosheets.

3.4.1 Rate charge-discharge test

First, the four materials were tested with rate charge-discharge to see their electrochemical performance and capacity. All the electrode were produced with the ratio of active material: conductive agent: binder as 5:4:1 to ensure the carbon black was enough to be coated on the active material. Then the electrodes were characterized by EC-lab electrochemistry workstation at 0.5C, 1C, 2C, 5C, 10C, 20C and 0.5C at last. Every sequence had three cycles, and the second cycles are plotted and compared in **Figure 3.10**.

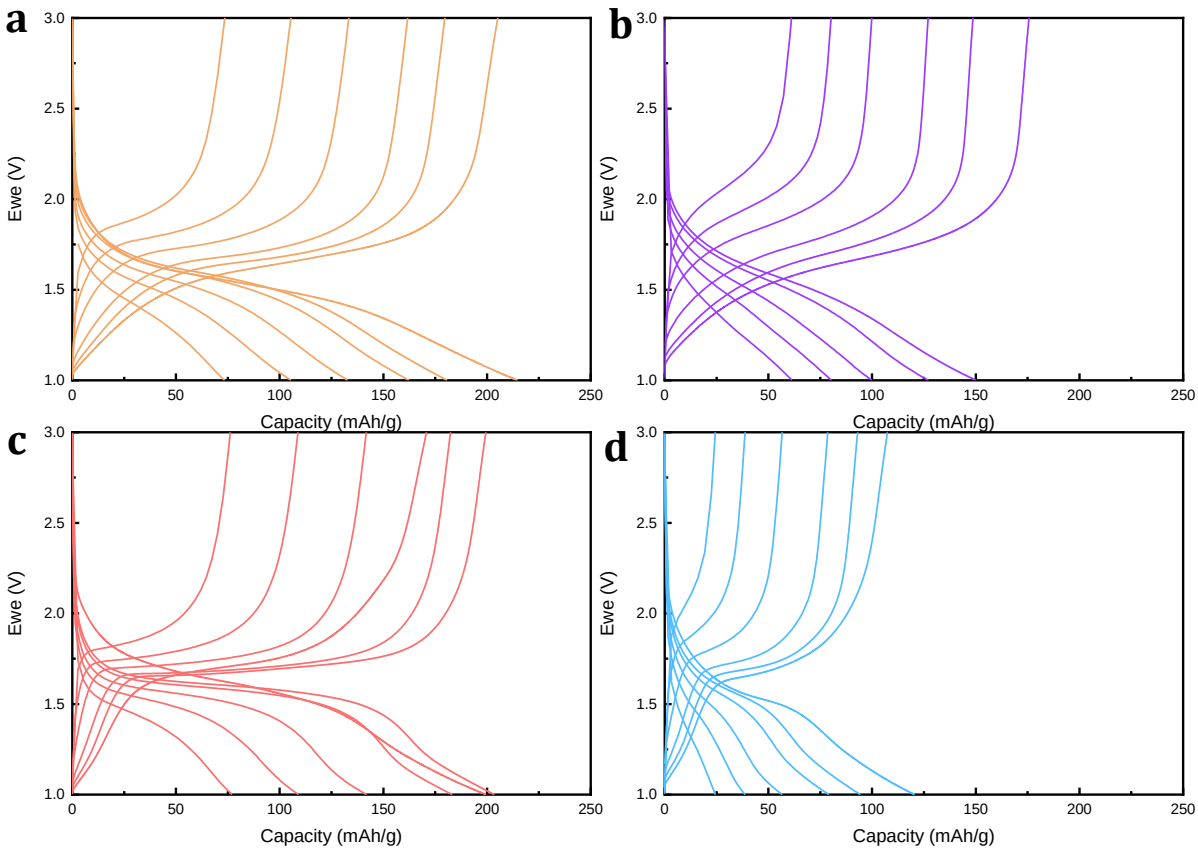

Figure 3.10 rate charge-discharge curves of 0.5C, 1C, 2C, 5C, 10C and 20C. (a) $TiNbO_5$ nanosheets, (b) Ti_5NbO_{14} nanosheets, (c) bulk $TiNbO_5$ and (d) bulk $H_3Ti_5NbO_{14}$. The black dash lines in every image was the 0.5C cycle curve after 20C.

The two nanosheets samples seem to have similar performances in the test, and the $TiNbO_5$ nanosheets show higher capacity at 0.5C with a capacity over 200 mAh/g while Ti_5NbO_{14} started with 175 mAh/g at 0.5C. Their capacity attenuated with the increasing of the C-rate, the $TiNbO_5$ remained its capacity for 72 mAh/g at 20C, while those of Ti_5NbO_{14} only had 61 mAh/g. We also performed another 0.5C at the end of test to examine the recovery of the capacity. The $TiNbO_5$ exhibit 182 mAh/g during the recovery cycle while the other nanosheets sample showed 157 mAh/g. The retention rates of the capacity of them were 91.0% and 89.7% respectively.

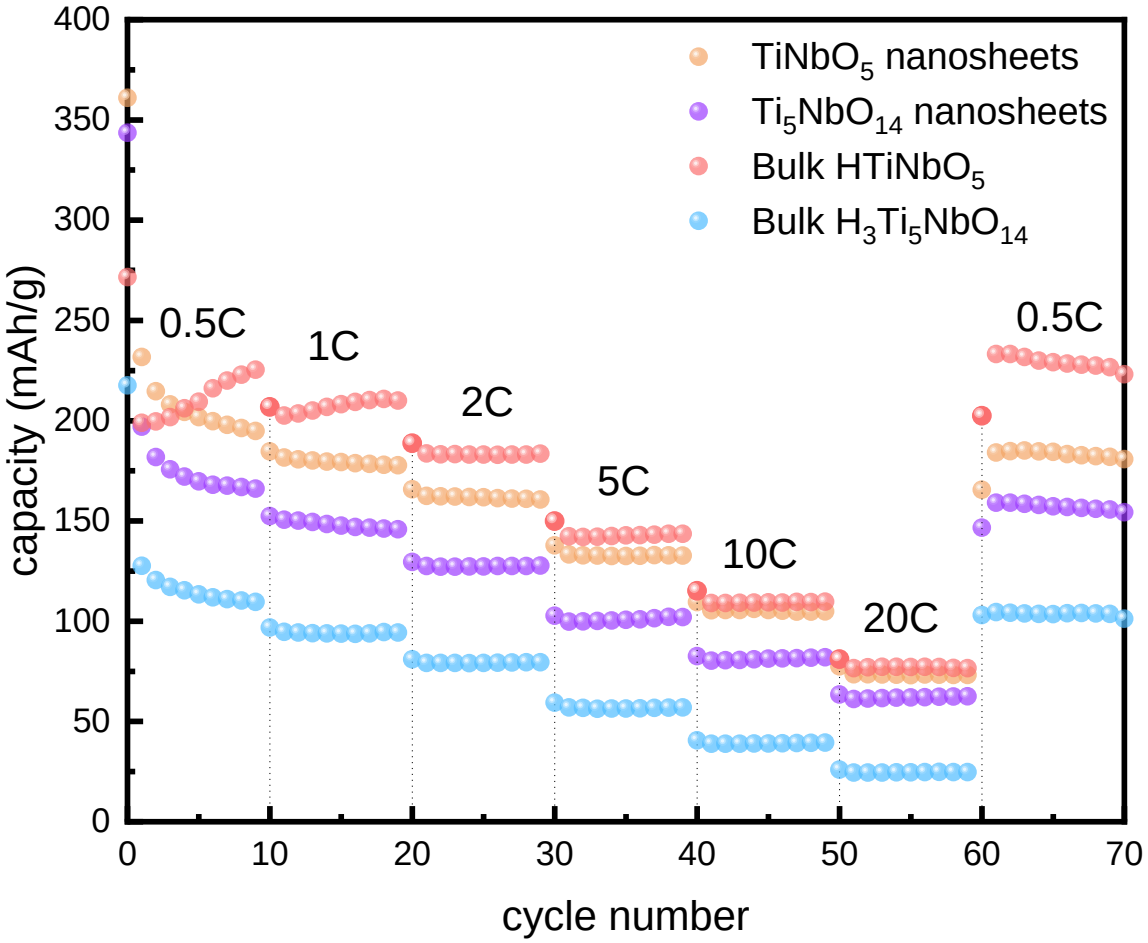

Figure 3.11 Capacity (charge) versus cycle number plot.

The bulk $HTiNbO_5$ shows abnormal behavior in the rate charge-discharge test as in **Figure 3.10c**. In the first cycle of 0.5C, it only had 170 mAh/g of capacity, which was lower than the capacities of 1C and 2C, however, most of the electrodes had highest capacity during the first three cycles. When we look into the capacity vs. cycle number plot in **Figure 3.11**, there was a unique increase occurred in the first ten cycles at 0.5C. A probable reason is that the access of electrolyte ions to the active materials surface after the first cycle became more easily. Initially electrolyte ions were not able to

reach all areas of the active electrode material. With further cycling electrolyte contacted the whole area of the electrode which increased the charge capacity. Due to the abnormal result of the test, the retention rate of the material's capacity was higher than 100% with a result that it had a capacity of 228 mAh/g at the end of the test.

The bulk $H_3Ti_5NbO_{14}$ had lowest lithium storage among the four electrodes. When the C-rate was 0.5, its capacity was only 107 mAh/g, and that of 20C was 24 mAh/g. The retention rate of the capacity was 94.4%. The performance was poor and the bulk $H_3Ti_5NbO_{14}$ was not qualified as an anode material.

It can also be observed that there were significant drops of the capacity from the first cycle to the second cycle in all the materials. This is because there were H atoms were in the crystals and nanosheets, and the Li^+ ion replaced the H atoms at the first cycle, therefore the lithium storage was high at the first cycle. After the replacement was done, the capacity became stable, and the stable capacity was the actual one.

In conclusion, the rank of the electrodes according to their lithium storage performance is: bulk $HTiNbO_5$ > $TiNbO_5$ nanosheets > Ti_5NbO_{14} nanosheets > bulk $H_3Ti_5NbO_{14}$. The bulk $HTiNbO_5$ and $TiNbO_5$ had similar capacity at 5C, 10C and 20C, and the $TiNbO_5$ nanosheets and Ti_5NbO_{14} nanosheets had close capacity at 20C.

3.4.2 Cyclic voltammetry

Cyclic voltammetry test can accurately analyze the electrode reaction of the TNO bulk and nanosheets in different voltage ranges.

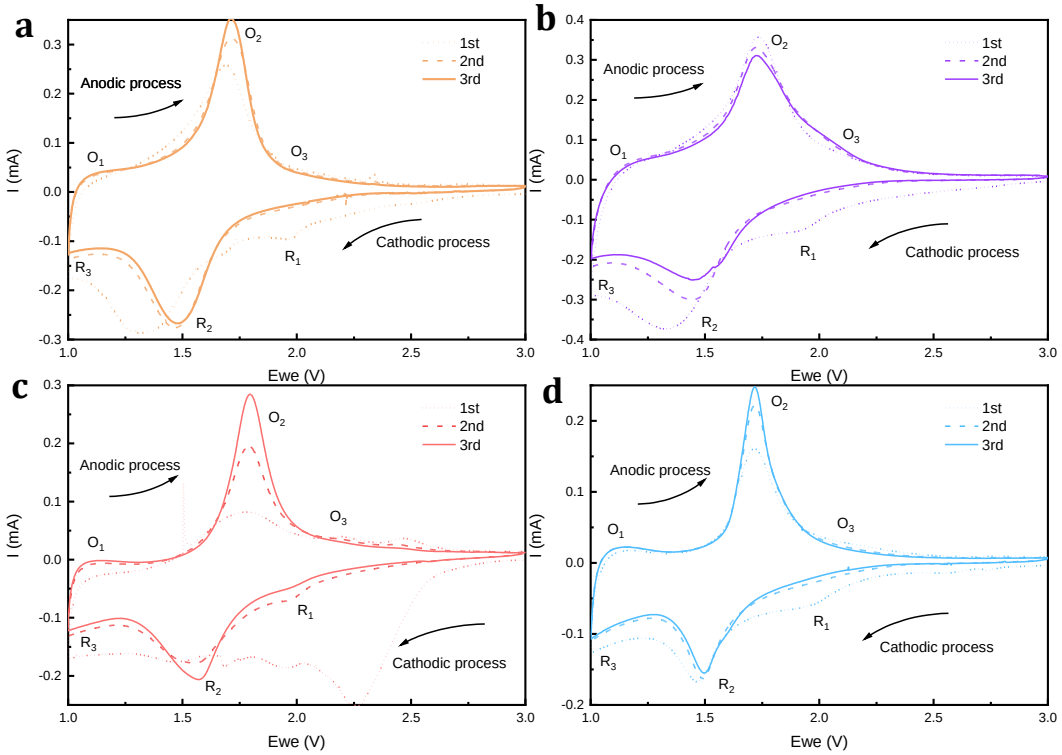

Figure 3.12 CV curves of (a) $TiNbO_5$ nanosheets, (b) Ti_5NbO_{14} nanosheets, (c) $HTiNbO_5$ bulk and (d) $H_3Ti_5NbO_{14}$ bulk on the first three cycles at a scan rate of 0.2 mV/s with a potential window of 1.0-3.0 V vs. Li^+/Li.

Figure 3.12 is the cyclic voltammetry curve of the first three cycles of all the electrodes, and the scan rate was 0.2 mV/s and the scan voltage range was 1.0 – 3.0 V (vs. Li^+/Li). As shown in **Figure 3.12**, the curves of the first three cycles were not overlapped especially the first cycle. There are some noise points in the **Figure 3.12a** and **Figure 3.12b**, which indicated the $TiNbO_5$ and $HTiNbO_5$ have unstable cycle performance.

It can also be seen from the figure that in the process of discharging and charging, as the voltage decreases and increases, three pairs corresponding redox peaks appear on the CV curve, which are O_1/R_3, O_2/R_2, and O_3/R_1 respectively. The first pair of O_3/R_1 corresponds to the Ti^{4+}/Ti^{3+} redox reaction near 1.9V; the second pair of O_2/R_2 corresponds to the Nb^{5+}/Nb^{4+} redox reaction near 1.6V, which is the strongest peak; and the third pair of O_1/R_3 corresponds to the Nb^{4+}/Nb^{3+} redox reaction near 1.3V. The O_3/R_1 peak is hard to be observed and it is only visible in the first cycles, which means the Ti^{4+}/Ti^{3+} redox reaction is not dominant during the charging and discharging, while the Nb^{5+}/Nb^{4+} redox reaction is the strongest and dominant reaction during the whole process.

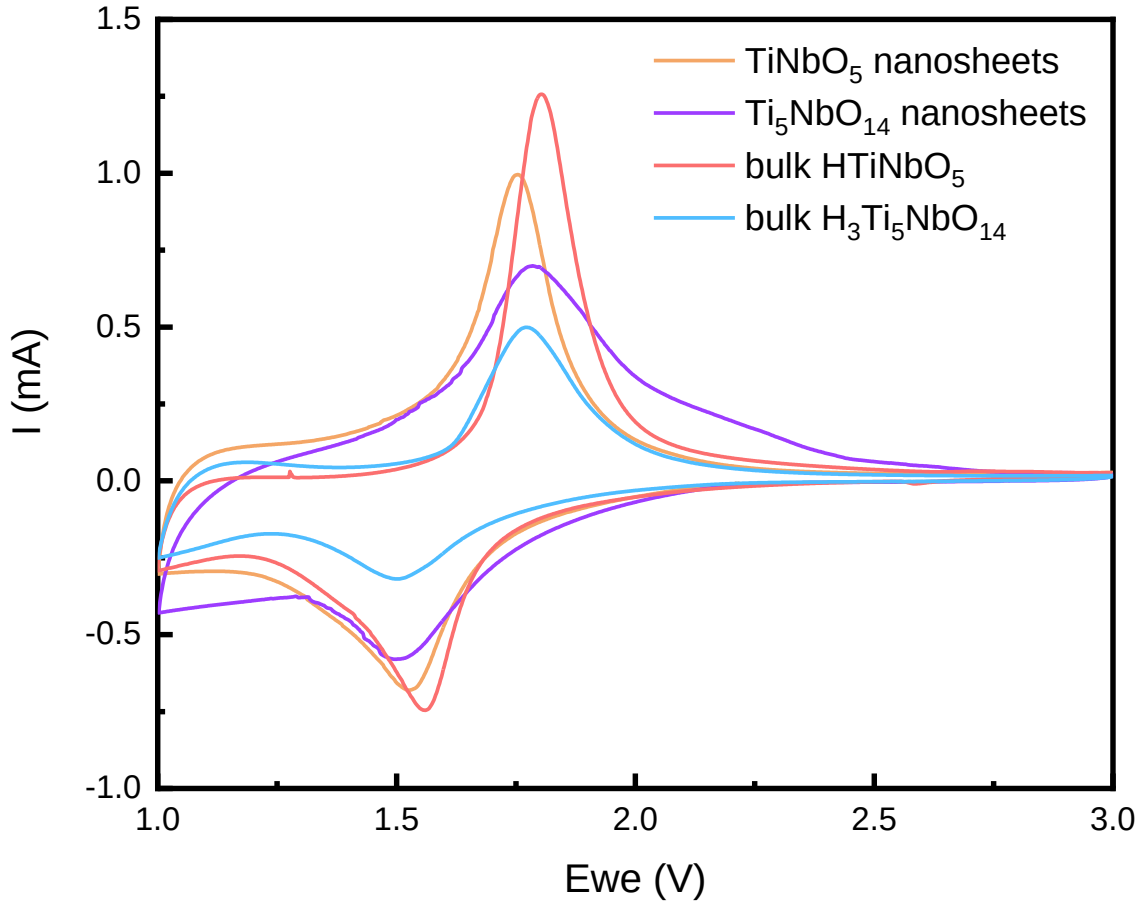

Figure 3.13 CV curves of $TiNbO_5$ nanosheets, Ti_5NbO_{14} nanosheets, $HTiNbO_5$ bulk and $H_3Ti_5NbO_{14}$ bulk at 0.6 mV/s between 1.0-3.0 V vs. Li^+/Li.

Another interesting point is the peak intensity and the location as in **Figure 3.13**. Comparing with the location of the O_2 peaks of Ti_5NbO_{14}, bulk $HTiNbO_5$ and bulk $H_3Ti_5NbO_{14}$, the polarization voltage of the O_2 peak of $TiNbO_5$ nanosheets electrode is shifted to left and reduced by 0.05V, indicating that the $TiNbO_5$ nanosheets promoted electron transfer slightly. At the same time, a smaller polarization voltage represents a more excellent lithium ion intercalation and de-intercalation performance of the electrode. In addtion, the bulk $HTiNbO_5$ exhibits greatest peak intensity, corresponding to the highest electrochemical performance. It is also noticeable that the width of peaks of $TiNbO_5$ nanosheets and bulk $HTiNbO_5$ is smaller than the other two electrodes and the O_3/R_1 peak is hard to be observed in them, which represents that Nb^{5+}/Nb^{4+} and Nb^{4+}/Nb^{3+} redox reactions are dominant in $TiNbO_5$ nanosheets and bulk $HTiNbO_5$.

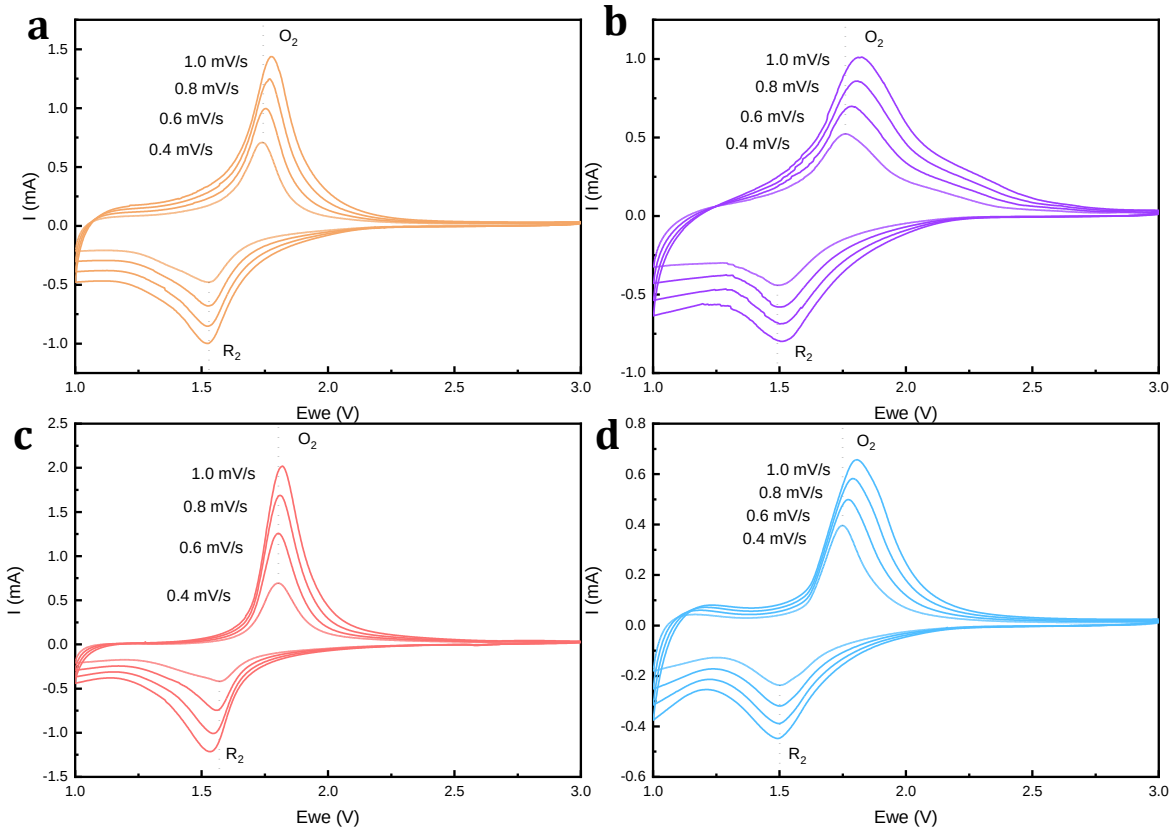

Figure 3.14 CV curves with the potential range from 1.0V to 3.0V vs. Li^+/Li at various scan rates of (a) $TiNbO_5$ nanosheets, (b) Ti_5NbO_{14} nanosheets, (c) $HTiNbO_5$ bulk and (d) $H_3Ti_5NbO_{14}$ bulk.

From the analysis in the previous section, it can be seen that during the charging and discharging processes of the TNO anode material, there are mainly three pairs of redox reactions. The kinetic characteristics of these three redox reactions also directly affect the electrochemical performance of the electrode. The electron reaction process mainly includes the following four processes[46,47]: (1) the transfer of electrons at the interface between the active material particles and the current collector; (2) the deintercalation of lithium ions in the solid phase of the active material particles; (3) the lithium ion at the solid-liquid phase interface between the active material particles and the electrolyte; and (4) the transfer of lithium ions in the electrolyte. In the above electrode reaction

process, the transfer of electrons and the transfer of lithium ions in the electrolyte are faster, and the transfer of lithium ions at the solid phase and solid-liquid two-phase interface is the speed control step in the electrode reaction process. The peak shape and peak position of the redox peak in the CV curves can show the kinetic characteristics of lithium ion diffusion in the electrode reaction system. Therefore, based on the mathematical analysis of the CV curve, the kinetic parameters during the electrode reaction can be analyzed. **Figure 3.14** shows the CV curves of electrodes in the potential range of 1.0 - 3.0V and at different scan rate (0.4, 0.6, 0.8 and 1.0 mV/s). The 0.2 mV/s scan results are not compared together in this section since their instability. It can be seen from the figure that there are obvious differences in the CV curves at different scanning speeds. The O_2/R_2 pair of redox peak position is selected as the research object due to its intensity. As the scan rate increased, the O_2 and R_2 peaks move towards higher and lower levels respectively. The deviation of the potential direction indicates the polarization phenomenon of this pair of redox reactions at the high scan rate.

3.4.2.1 Calculation of lithium ion coefficient from CV curves

From **Figure 3.14**, we can get the peak current i_p corresponding to the O_2/R_2 redox peak of all electrodes at different scan rate v, and thus i_p and $v^{0.5}$ can be obtained. The relationship diagram is shown in **Figure 3.15**. Clearly, there is a linear relationship between i_p and $v^{0.5}$, indicating that the electrochemical reaction process was limited by the diffusion process. Therefore, the intercalation and deintercalation of lithium ions in the O_2/R_2 redox process can be regarded as a reversible reaction. Based on this, the Randles-Sevcik equation (Equation 3-1) that uses the electrochemical reaction to control the current under semi-infinite linear diffusion conditions can calculate the apparent diffusion coefficient of lithium ions[48].

$$i_p = kn^{\frac{3}{2}}SCD^{0.5}v^{0.5} \tag{3-1}$$

Where i_p is the peak current, k is a constant of 2.69×10^5 with units of C mol^{-1} $v^{-0.5}$, n is the number of transferred electrons, S is the area of the electrode immersed in the electrolyte (cm^2), C is the molar analyte concentration of lithium ion in solid (mol/L), which is estimated by the number of lithium ion per unit cell , D is the apparent diffusion coefficient of lithium ions (cm^2 s^{-1}) and v is the scan rate (V s^{-1}).

According to the calculation, the results were listed in **Table 3.2**:

Active materials	Anodic/Cathodic slope(mA $v^{-0.5}$ $s^{-0.5}$)	Anodic/Cathodic D_{Li^+} (cm^2 s^{-1})
$TiNbO_5$ nanosheets	63.071 / -44.840	4.34×10^{-10} / 2.19×10^{-10}
Ti_5NbO_{14} nanosheets	42.029 / -30.466	1.71×10^{-12} / 8.99×10^{-13}
$HTiNbO_5$ bulk	114.458 / -68.736	1.39×10^{-9} / 5×10^{-10}
$H_3Ti_5NbO_{14}$ bulk	22.476 / -18.165	4.73×10^{-13} / 3.09×10^{-13}

Table 3.2 D_{Li^+} values of electrodes calculated from CV curves obtained at different scan rates using Randles-Sevcik equation.

Table 3.2 compares the D_{Li^+} values of the electrodes made with the four active materials based on the same CV test method and the Randles-Sevcik equation. It can be seen that $TiNbO_5$ and $HTiNbO_5$ exhibited relatively excellent lithium ion diffusion abilities. And it is worth noticing that from the lithium ion diffusion coefficient data listed in the table, the lithium ion intercalation in the reduction process was the speed control step of the entire electrochemical reaction.

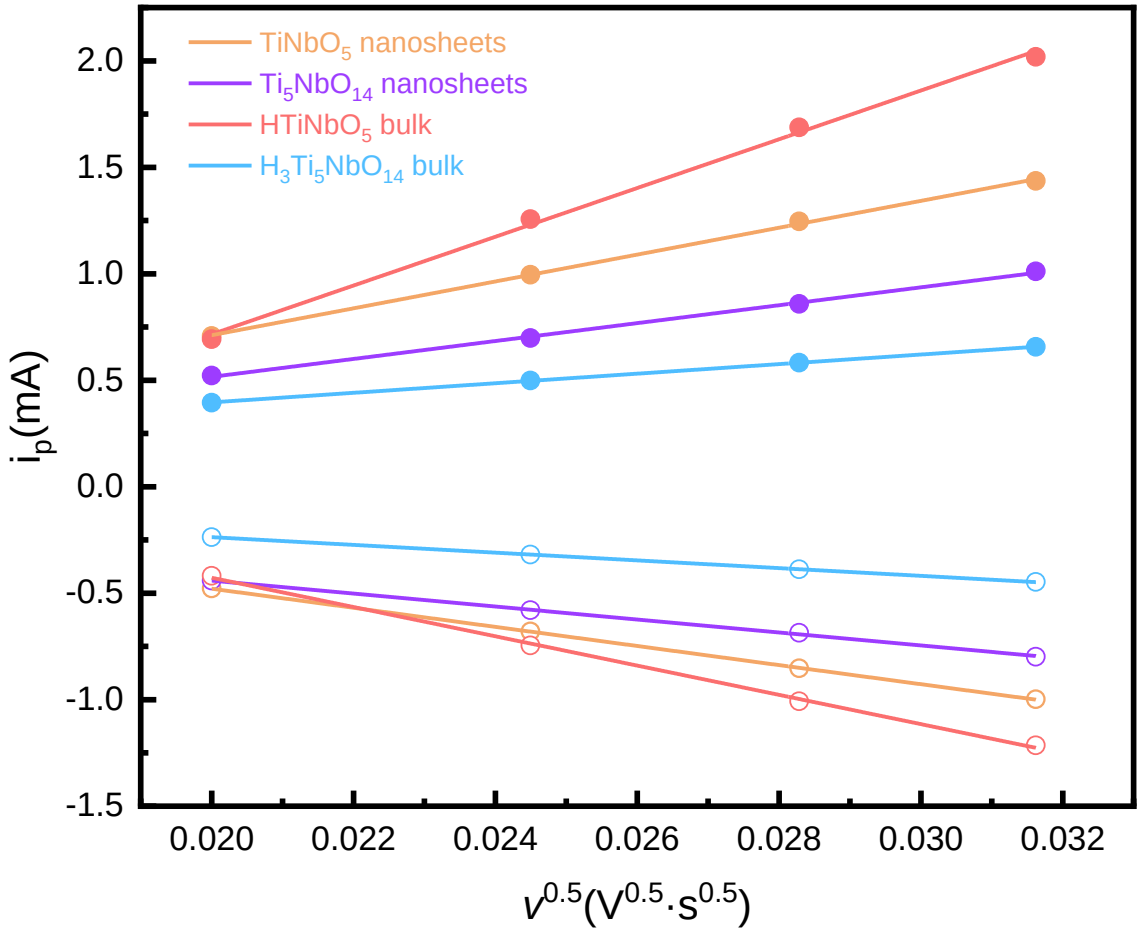

Figure 3.15 Peak currents i_p versus square roots of scan rate.

3.4.2.2 Pseudocapacitance

The charge storage modes of electrode materials usually include the following three[49]: (1) the capacity contributed by the induced current during the lithium ion intercalation process (the Faraday process controlled by solid phase diffusion, and the general bulk battery materials mainly stores the capacity in this way.); (2) the capacitance provided by the Faraday process of transfer from the surface or near the surface of the electrode material, which called pseudocapacitance; (3) capacity provided by the interaction of the electric double layer capacitance based on the ion absorption and desorption of the non-Faraday process with the absence of induced current. According to the above mechanism, by analyzing the CV curves of the electrodes at different scan rates (**Figure 3.14**) and **formula 3-2**[50,51] to match the scan rate and current, we can judge whether the dominant process of current response/charge transfer in the above CV test voltage range was diffusion control (i_{diff}) or surface control (i_{cap}).

$$i(V) = i_{diff} + i_{cap} = av^b \tag{3-2}$$

Take the logarithm of both sides of the above equation, we can get:

$$logi(V) = loga + blogv \tag{3-3}$$

Therefore, by fitting the current logarithm of the specific voltage at different scan rates and the logarithm of the scan rate, the b value can be obtained through the slope of the straight line.

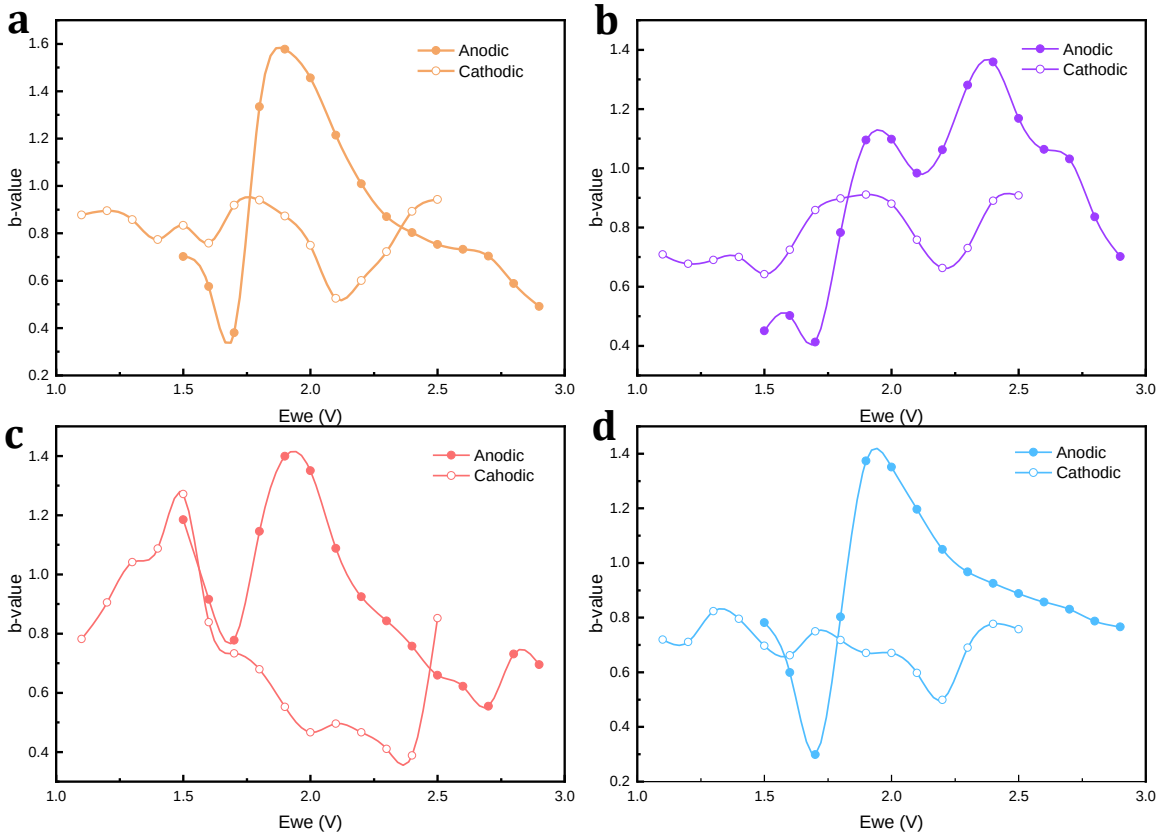

Figure 3.16 b values are plotted versus potential for (a) $TiNbO_5$ nanosheets, (b) Ti_5NbO_{14} nanosheets, (c) $HTiNbO_5$ bulk and (d) $H_3Ti_5NbO_{14}$ bulk.

For the redox reaction controlled by semi-infinite diffusion, if b=0.5, that is the current i changes with v to the power of 0.5, then the reaction is diffusion controlled, which is a battery behavior; if b=1, the current i changes linearly with v, then the reaction is surface process controlled, which is a pseudocapacitance behavior. In the same way, if the b-value is between 0.5 and 1, it means that the charge transfer process is a process controlled by both diffusion and surface, and the electrode behavior shows a behavior between the battery and the capacitor.

In this section, the O_2/R_2 redox process is selected as the study object. **Figure 3.16** shows the value of b calculated from the relationship between peak current and scan rate at different potential. As we can see in the **Figure 3.16 a, b and d**, b-values of cathodic process fluctuated around 0.8, which indicated the charge transfer in R_2 reduction processes of $TiNbO_5$, Ti_5NbO_{14}, and $H_3Ti_5NbO_{14}$ were mixed control processes. The b-value of $HTiNbO_5$ was different from the others, indicating the $HTiNbO_5$ behaved as battery at 1.5V and as capacitance at 2.0-2.5V. Since the R_2 peak is around 1.5V, and R_1 peak is around 2.25V, the b-values reveal that the R_2 peak is surface process controlled and R_1 peak was diffusion process controlled.

However, the anodic b-values show totally different trends with the cathodic ones. When we look into the region where O_2 peaks occurs, the b-values are all over 1.0, which means the O_2 oxidation is

a surface controlled process. The value was over 1.0 is because the polarization and the shift of the O_2 peak. In addition, it is found that, in the O_2/R_2 redox process, the cathodic b-value is smaller than the anodic one, indicating that the intercalation kinetics of lithium ions during the charge transfer process was more difficult than the deintercalation. This result is consistent with the comparison result of the D_{Li^+} values based on the Randles-Sevcik equation. Another interesting foundation was that the anodic and cathodic b-values were not approximate compared to most cases. I assumed the unique kinetics can be ascribed to the special crystal structure of TNO and HTNO after electrochemical reduction.

Despite of **Equation 3-2**, we can also quantitatively analyzed the contribution of capacitance effect and diffusion controlled process respectively by analyzing the CV curves at different scan rates. According to the previous sections, we know that $i_{cap} = k_1 v$ (capacity contribution of capacitance effect), $i_{diff} = k_2 v^{0.5}$ (capacity contribution of diffusion process). Therefore, we can get the following formula:

$$i(V) = i_{diff} + i_{cap} = k_1 v + k_2 v^{0.5} \tag{3-4}$$

Where i(V) is the current at certain potential. The above equation can be transformed into:

$$i(V)/v^{0.5} = k_1 v^{0.5} + k_2 \tag{3-5}$$

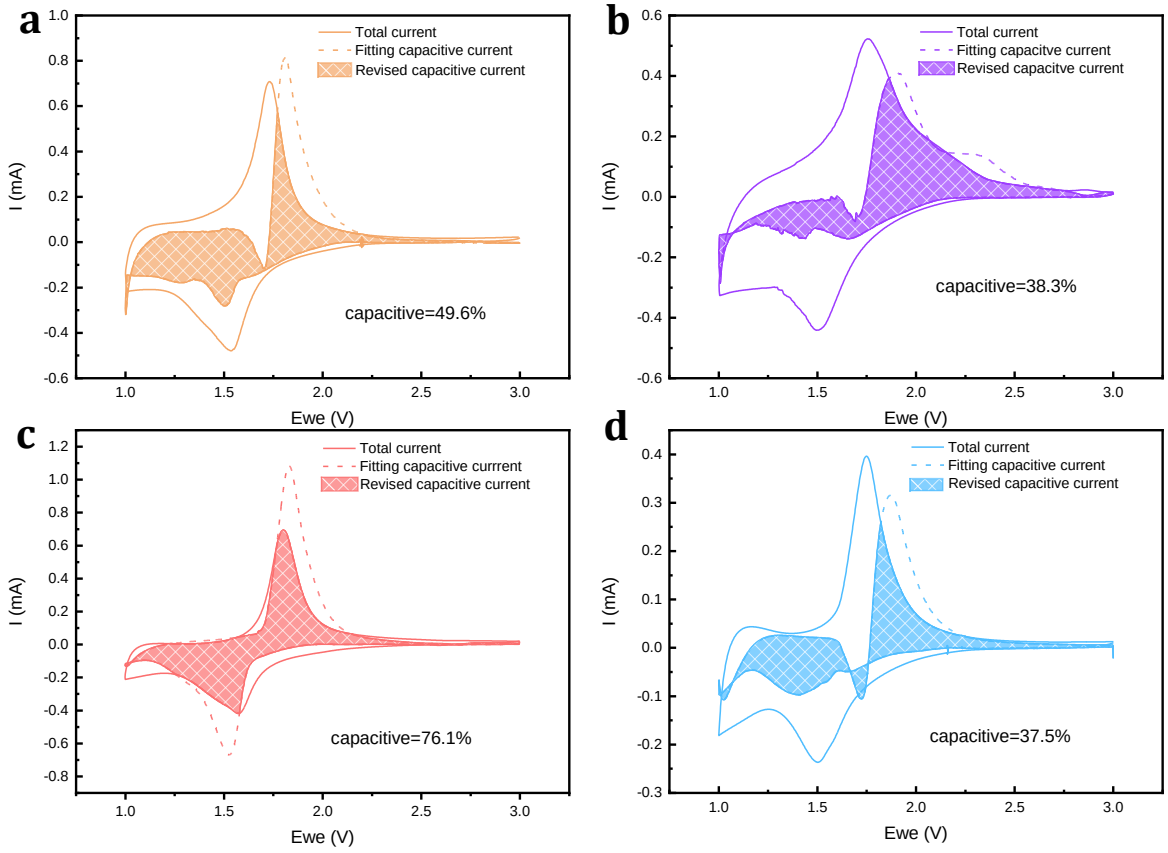

Figure 3.17 The percentage of capacitive current at 0.4 mV/s scan rate for (a) $TiNbO_5$ nanosheets, (b) Ti_5NbO_{14} nanosheets, (c) $HTiNbO_5$ bulk and (d) $H_3Ti_5NbO_{14}$ bulk.

A straight line is obtained by fitting $i(V)/v^{0.5}$ to $v^{0.5}$ at a certain potential at difference sweep speeds (0.4, 0.6, 0.8, 1.0 mV/s), and the slope and intercept of the straight line are k_1 and k_2 respectively. Then the k_1v and $k_2v^{0.5}$ are calculated respectively and the capacity contribution of the diffusion process and the pseudocapacitance effect at the potential can be obtained. Therefore, the k1 and k2 values at different potentials in the CV test voltage window are calculated, and then the contribution of the capacity can be analyzed.

Figure 3.17 shows the discrimination result of electrodes pseudocapacitance/diffusion process capacity contribution at 0.4 mV/s scan rate. The shaded part in the figure represents the capacity contributed by the capacitive effect. It can be seen that about 49.6%, 38.3%, 76.1%, 37.5% respectively of the electrodes' capacities are contributed by the capacitive effect, that is, the lithium ion deintercalation pseudocapacitance on and near the surface of TNO and HTNO. The significant pseudocapacitance effect of $HTiNbO_5$ bulk highlights the dynamic performance of lithium ion deintercalation, which is beneficial to the performance of electrode materials at high current density rates.

However, it is obvious that the fitting results had large error as the dash lines in the figure. The area of the dash lines exceeds the original CV curves. And in this study, I revised the fitting curves with deleting the area over the original CV curves. This shows the fitting method of the equation above still has an error, and cannot calculated the accurate capacity percentage.

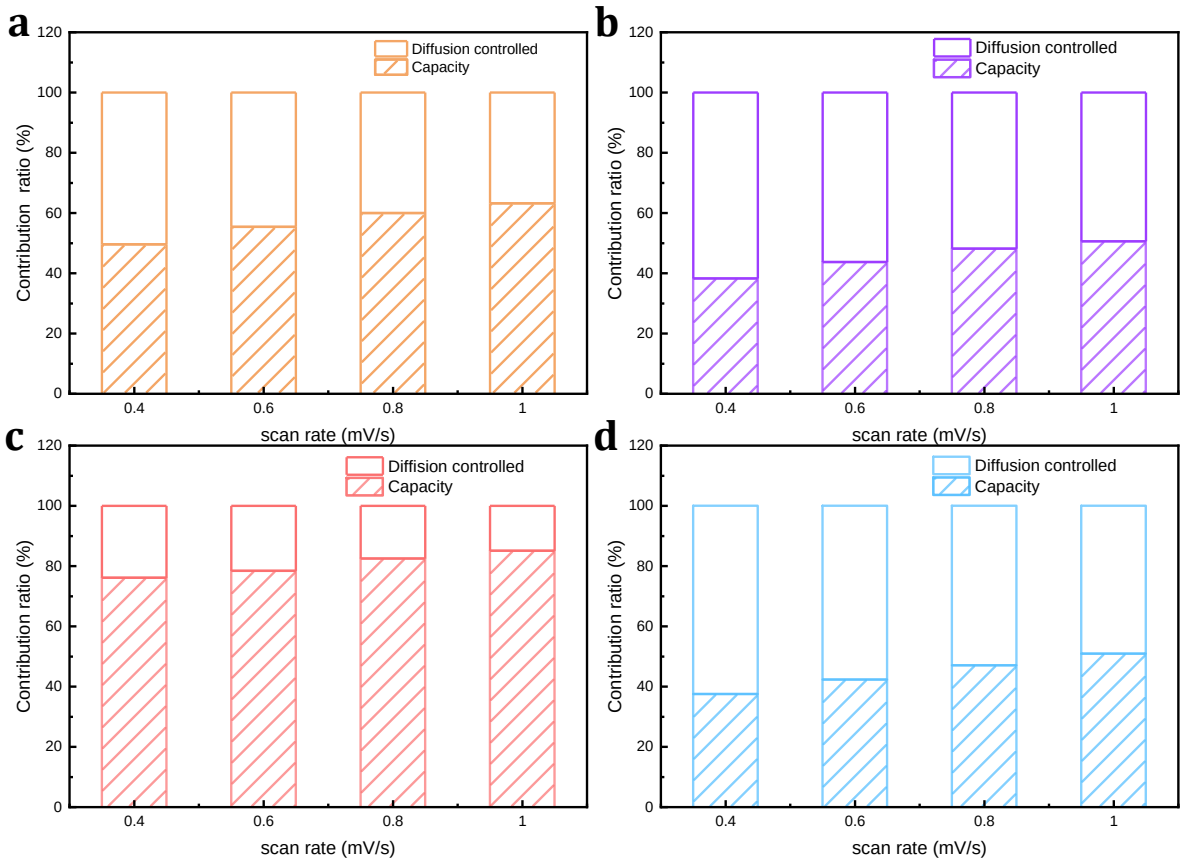

Figure 3.18 Contribution ratio of capacity/diffusion to current at different scan rates for (a) $TiNbO_5$ nanosheets, (b) Ti_5NbO_{14} nanosheets, (c) $HTiNbO_5$ bulk and (d) $H_3Ti_5NbO_{14}$ bulk.

Figure 3.18 shows the variation of the capacity ratio of the diffusion controlled and pseudocapacitance controlled in the electrodes with the scan rates. As shown in the figure, the capacity contribution ratio of pseudocapacitance effect shows an increasing trend in all electrodes as the scan rate gradually increased from 0.4 mV/s to 1.0 mV/s. The capacity contribution ratio of pseudocapacitance effect for $HTiNbO_5$ bulk is 76.1%, 78.4%, 82.5% and 85.1% respectively. Obviously, with the increase of the scan rate, the capacity contributed by the surface pseudocapacitance effect gradually dominates, which is also the premise for the good high-rate performance of the electrode material. At the 0.4 mV/s scan rate, the $HTiNbO_5$ bulk already shows superior pseudocapacitance contribution ratio which gives $HTiNbO_5$ bulk better rate performance than the other three samples because of the faster charge-discharge mechanism of the capacitance controlled material. The electrode made with HTi_5NbO_{14}, which has the poorest performances in the study, has also lowest pseudocapacitance contribution, which consistent with the previous results.

3.4.3 Electrochemical impedance spectroscopy

In order to further study the kinetic characteristics of TNO nanosheets and HTNO bulks during the electrode reaction process of lithium ion transfer at the interface, the EIS tests were conducted on the four materials. The amplitude was 10mV, and the frequency range was 0.1MHz to 0.01 Hz. Before the EIS test, the batteries were performed for a rate charge-discharge test and then the voltage was stabilized after rest.

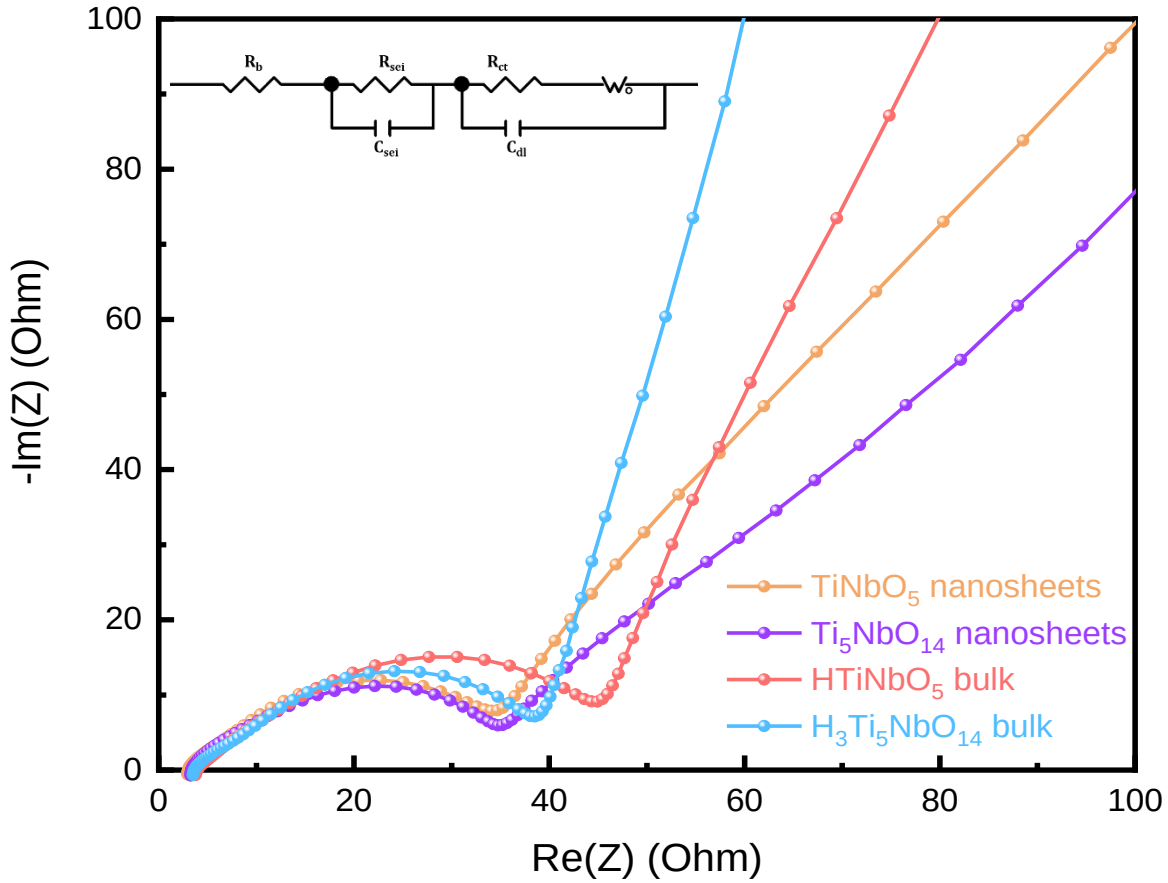

Figure 3.19 Nyquist plots of the $TiNbO_5$, Ti_5NbO_{14}, $HTiNbO_5$ and $H_3Ti_5NbO_{14}$ (inset: corresponding equivalent circuit model).

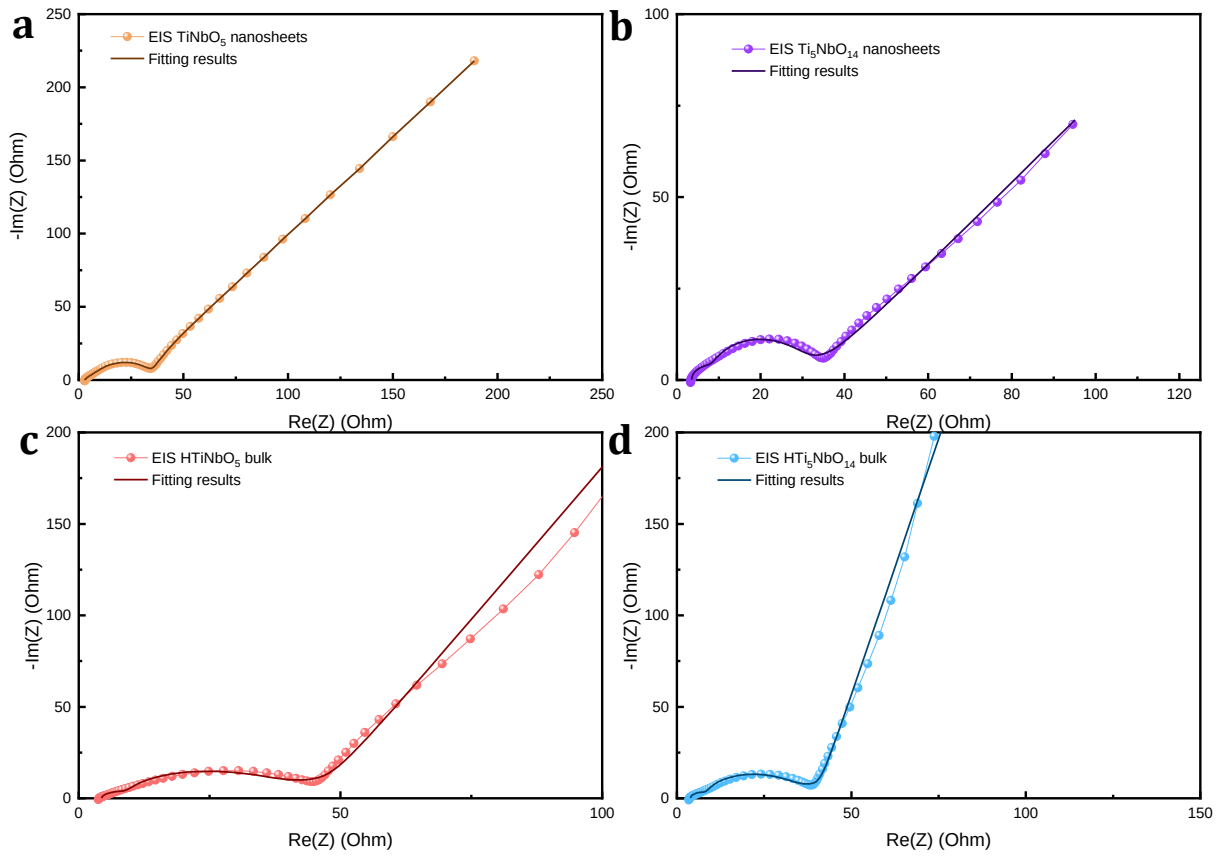

Figure 3.20 EIS data and fitting results of (a) $TiNbO_5$ nanosheets, (b) Ti_5NbO_{14} nanosheets, (c) $HTiNbO_5$ bulk and (d) $H_3Ti_5NbO_{14}$ bulk.

As shown in **Figure 3.19**, the EIS spectra of the four electrodes are composed of two semicircles in the high and intermediate frequency region and a straight line in the low frequency region. In the above figure, the ohmic resistance R_b is where the impedance curves intersect the x-axis. The diffusion resistance of lithium ions (R_{sei}) in the solid electrolyte is embodied as a semicircle in the high frequency region; the transfer resistance of the charge (R_{ct}) is embodied as a semicircle in the intermediate frequency region; and the diffusion resistance of the lithium ions in the solid phase crystal lattice (W) is expressed as a straight line in the low frequency region. The equivalent circuit of impedance is shown in the inset. The fitting results are compared in **Figure 3.20** to the equivalent circuit is as below:

Active materials	$R_b(\Omega)$	$R_{sei}(\Omega)$	$R_{ct}(\Omega)$
$TiNbO_5$ nanosheets	3.185	3.836	17.74
Ti_5NbO_{14} nanosheets	3.532	4.721	16.57
$HTiNbO_5$ bulk	4.395	4.898	25.37
$H_3Ti_5NbO_{14}$ bulk	3.929	4.555	23.62

Table 3.3 Fitting results of EIS for four materials according to the equivalent circuit.

The diameters of the nanosheets samples are obviously smaller than the bulk samples, so the corresponding R_{ct} of nanosheets is smaller. And according to the fitting results in **Table 3.3**, they

show similar ability for transportation of lithium ions at the interface between nanosheets/bulks and electrolyte. It can be referred from the straight lines in the low frequency region that the slopes of the lines of bulk electrodes are steeper than those of nanosheets, indicating that the their W are smaller and the lithium ions diffuse faster in the bulk electrodes. In summary, the nanosheets have smaller charge transfer resistance but larger diffusion resistance, and the bulks have higher charge transfer resistance and smaller diffusion resistance.

3.4.4 Long cycling life

In order to characterize the high rate performance and the cycle life of the four active materials, long cycling tests of 2×500 cycles were performed on the four active materials at high C-rates of 10C and 20C respectively. The test results are shown in **Figure 3.21**.

The $TiNbO_5$ nanosheets exhibit extremely unstable performance. The capacity of it violently fluctuates around 90 mAh/g at 10C, and its capacity at 20C also waves at approximately 60 mAh/g. The $HTiNbO_5$ bulk shows fantastic performance during the long cycling test. Its capacity creeps from 53 mAh/g to 129 mAh/g at the end of 10C, which is similar to its behavior in rate charge-discharge test at 0.5C. In addition, the performance of $HTiNbO_5$ bulk at 20C is also not so stable, it is visible that the capacity had little fluctuations at 20C.

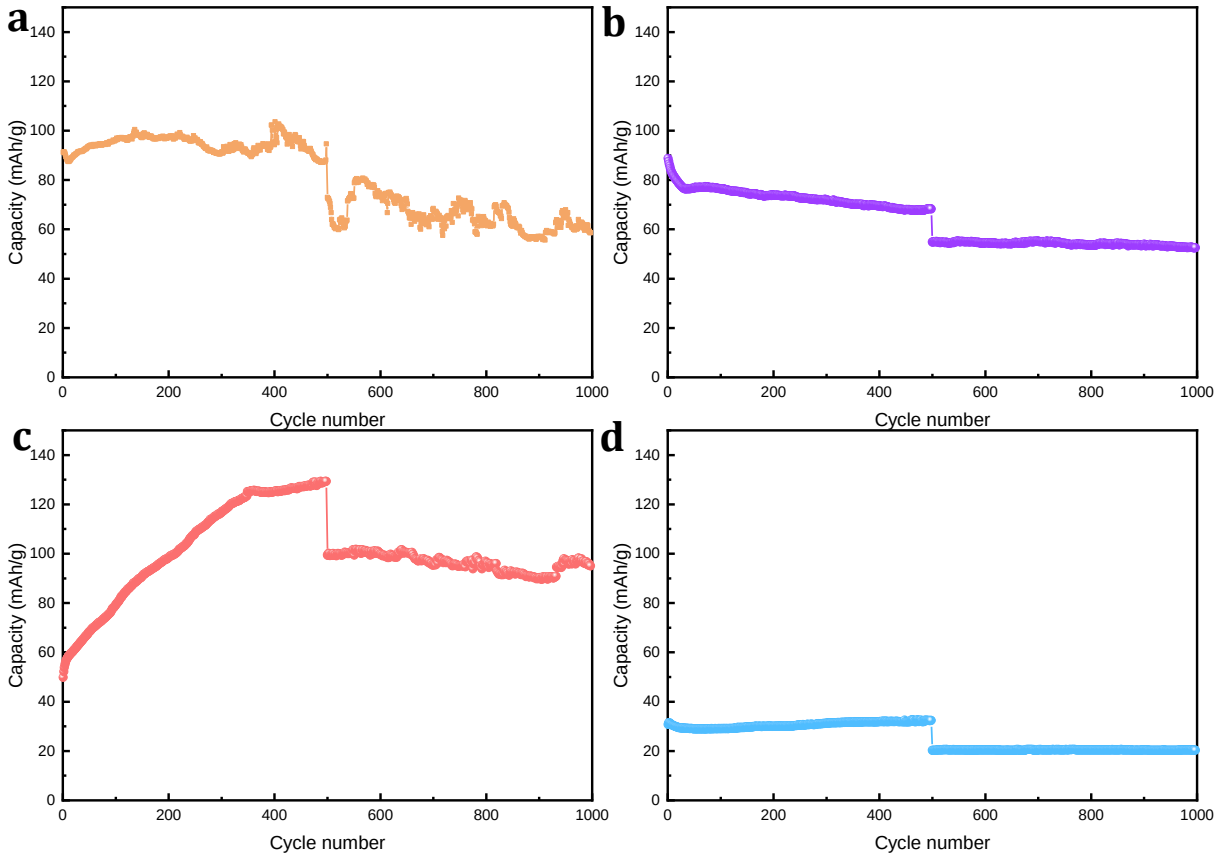

Figure 3.21 Long cycling test results (first 500 cycles: 10C and last 500 cycles: 20C) of (a) $TiNbO_5$ nanosheets, (b) Ti_5NbO_{14} nanosheets, (c) $HTiNbO_5$ bulk and (d) $H_3Ti_5NbO_{14}$ bulk.

The Ti_5NbO_{14} nanosheets and $H_3Ti_5NbO_{14}$ show stable performance compared to the 1:1 ratio electrodes. The Ti_5NbO_{14} nanosheets maintain a specific capacity of 68.4 mAh/g after the 500 cycles at 1C, which correspond to a retention rate of 77%. Its retention rate at 20C for 500 cycles is 96%. The HTi_5NbO_{14} bulk has perfect stability but poor specific capacity. The retention rates of HTi_5NbO_{14} bulk are almost 100%, however its capacities are 30 mAh/g and 20 mAh/g at 10C and 20C respectively, which are the same results in the previous rate charge-discharge test.

According to previous analysis in CV, the dominant redox reaction in the process is the Nb^{5+}/Nb^{4+} reaction. In the compounds of Ti : Nb ratio of 1:1 ($TiNbO_5$ nanosheets and $HTiNbO_5$ bulk), the percentage of Nb in the oxide is higher than that of compounds in 5 : 1 ratio, therefore the redox reaction and the lithium ion diffusion speed in the $HTiNbO_5$ is faster than H_3TiNbO_{14} bulk and the speed in $TiNbO_5$ nanosheets is faster than the Ti_5NbO_{14} nanosheets.

In principle, the nanosheets samples have higher specific area than bulk samples, which should lead to a higher specific capacity. However, in the tests, the nanosheets samples show less capacity than the bulk samples. The reason why the nanosheets electrodes cannot perform as we thought might be the morphology of them. As we can see in the **Figure 3.3**, the fluffy layered structure shows the nanosheets have inner area, which cannot be coated with carbon black, so that their capacities are not the best.

4 Conclusion

In this study, I took the $TiNbO_5$ nanosheets, Ti_5NbO_{14} nanosheets, $HTiNbO_5$ bulk and $H_3Ti_5NbO_{14}$ bulk as research objects. The exfoliation processes were successfully explored to fabricate the nanosheets with higher electrochemical performance. After that, the bulk materials and the nanosheets exfoliated by the optimized methods were compared in electrochemical characterization and discussed. The main conclusions of this project are listed as below:

1) For the exfoliation process of $TiNbO_5$ nanosheets, instead of the previous method as drying the protonated powder at 60℃ in a vacuum oven and calcining the nanosheets in oven, they were dried at room temperature after protonation and the exfoliated solution (with TBAOH) was added by certain amount of H^+ to neutralize the TBAOH in the reaction. At last, the nanosheets were washed and dried at room temperature in a vacuum oven.

   This process can improve the capacity performance due to the following two reasons:(a) drying the protonated powder at high temperature in a vacuum atmosphere lets the H^+ evaporated quickly and the spacing of the $HTiNbO_5$ layered structure intends to decrease; and (b) calcining the nanosheets with TBAOH at 450℃ might burn out the TBA^+ between the layers and the nanosheets get restacked again.

2) For the exfoliation process of Ti_5NbO_{14} nanosheets, LB deposition was applied to construct a Si substrate with nanosheets on it. After characterizing the nanosheets on Si wafers with different exfoliation conditions, the most efficient exfoliation was selected: mix 0.4g $H_3Ti_5NbO_{14}$, 2.11 mL TBAOH and 80 mL DI water to react for 24 hours.

3) For the rate charge-discharge test, the capacities of four electrodes were compared. The rank is: $HTiNbO_5$ bulk > $TiNbO_5$ nanosheets >Ti_5NbO_{14} nanosheets > H_3TiNbO_5 bulk.

4) For the cyclic voltammetry, the lithium ion diffusion coefficients were calculated, which correspond to the capacity performance of them. The $HTiNbO_5$ bulk has highest diffusion coefficient as 1.39×10^{-9} cm^2 s^{-1}. The high lithium ion diffusion coefficient represents that it had better capacity and better performance at high C-rate.

   The pseudocapacitance was also analyzed by the CV curves. The results of the contribution ratio of pseudocapacitance also confirmed the previous reults of rate charge-discharge tests. The HTiNbO5 bulk has higher pseudocapacitance at low scan rate than the other three samples which makes it perform best due to the faster charge-discharge mechanism of the capacitance controlled material.

5) For the electrochemical impedance spectroscopy, the EIS data were fitted by Zview and the fitting data show the nanosheets had smaller charge transfer resistance but larger diffusion resistance, and the bulks had higher charge transfer resistance and smaller diffusion resistance.

6) For the long cycling test, the $TiNbO_5$ nanosheets exhibit unstable performance with a specific capacity of ~90 mAh/g at 10C. In contrast, the Ti_5NbO_{14} and $H_3Ti_5NbO_{14}$ have very stable performance and retention rate, however their capacities are not as high as $TiNbO_5$ nanosheets. The $HTiNbO_5$ has fantastic performance in the long cycle life test, its capacity is the highest among the four samples. This is because the Nb5+/Nb4+ redox reaction is the controlled reaction in the process, and for Ti : Nb = 1 : 1 samples, they have better performance due to the higher Nb percentage so that the lithium diffusion is faster. The performance of nanosheets samples is not good as we expected because their fluffy layered structure makes them have more inner area, which cannot be coated with carbon black and the charge transfer and lithium diffusion are slower.

5 Outlook and recommendations

Combining research progress and current social hotspots, the following prospects can be put forward:

1) As the lithium ion diffusion coefficient calculation in Chapter 3.4.2.1, the cathodic lithium ion diffusion coefficients were smaller than anodic ones, there might be further modification for the HTNO and TNO which can improve the intercalation kinetics of lithium ion at cathodic process.
2) Further research on the mechanism of the increasing capacity of $HTiNbO_5$ should be carried on to figure out the mechanism of the unique phenomenon.
3) Synthesis method of nanosheets should be optimized to reduce the inner area.
4) More consideration should be given to the design and construction of TNO electrodes from the perspective of industrial production to optimize the production process and reduce the production cost.
5) With the continuous commercialization of folding mobile phones and smart wearable electronic devices, flexible batteries as a part of energy storage devices will also usher in the growth of consumer demand. Therefore, it is urgent to develop high-performance flexible battery devices that can be compatible and resistant to bending.

Reference

[1] Looney, B. (2020). Statistical Review of World Energy, 2020.

[2] Mai, L., Tian, X., Xu, X., Chang, L., & Xu, L. (2014). Nanowire electrodes for electrochemical energy storage devices. *Chemical reviews*, *114*(23), 11828-11862.

[3] Whittingham, M. S. (1976). Electrical energy storage and intercalation chemistry. *Science*, 192(4244), 1126-1127.

[4] Tarascon, J. M., & Armand, M. (2011). Issues and challenges facing rechargeable lithium batteries. *Materials for sustainable energy: a collection of peer-reviewed research and review articles from Nature Publishing Group*, 171-179.

[5] Murphy, D. W., Di Salvo, F. J., Carides, J. N., & Waszczak, J. V. (1978). Topochemical reactions of rutile related structures with lithium. *Materials Research Bulletin*, 13(12), 1395-1402.

[6] Lazzari, M., & Scrosati, B. (1980). A cyclable lithium organic electrolyte cell based on two intercalation electrodes. *Journal of The Electrochemical Society*, 127(3), 773.

[7] Nagaura, T. (1990). Lithium ion rechargeable battery. *Progress in Batteries & Solar Cells*, 9, 209.

[8] Thackeray, M. M., Wolverton, C., & Isaacs, E. D. (2012). Electrical energy storage for transportation—approaching the limits of, and going beyond, lithium-ion batteries. *Energy & Environmental Science,* 5(7), 7854-7863.

[9] Goodenough, J. B., & Kim, Y. (2010). Challenges for rechargeable Li batteries. *Chemistry of materials*, 22(3), 587-603.

[10] van Schalkwijk, W., & Scrosati, B. (Eds.). (2007). *Advances in lithium-ion batteries*. Springer Science & Business Media.

[11] Barin, I. (1989). Thermochemical data of pure substances. *VCH*.

[12] Lide, D. R. (Ed.). (2004). *CRC handbook of chemistry and physics (Vol. 85)*. CRC press.

[13] Speight, J. G. (2017). *Lange's handbook of chemistry*. McGraw-Hill Education.

[14] MEV Team. (2008). A guide to understanding battery specifications. *Massachusetts Institute of technology, USA, Tech. Rep*.

[15] Aurbach, D., Zinigrad, E., Teller, H., & Dan, P. (2000). Factors which limit the cycle life of rechargeable lithium (metal) batteries. *Journal of The Electrochemical Society*, 147(4), 1274.

[16] Fricke, J., & Borst, W. L. (2013). *Essentials of Energy Technology: Sources, Transport, Storage, Conservation Chapter 8*. John Wiley & Sons.

[17] Bruce, P. G., Scrosati, B., & Tarascon, J. M. (2008). Nanomaterials for rechargeable lithium batteries. *Angewandte Chemie International Edition*, 47(16), 2930-2946.

[18] Jiao, F., Harrison, A., Hill, A. H., & Bruce, P. G. (2007). Mesoporous Mn_2O_3 and Mn_3O_4 with crystalline walls. *Advanced Materials*, 19(22), 4063-4066.

[19] Okubo, M., Hosono, E., Kim, J., Enomoto, M., Kojima, N., Kudo, T., ... & Honma, I. (2007). Nanosize effect on high-rate Li-ion intercalation in $LiCoO_2$ electrode. *Journal of the American chemical society*, 129(23), 7444-7452.

[20] Dominko, R., Bele, M., Gaberscek, M., Remskar, M., Hanzel, D., Pejovnik, S., & Jamnik, J. (2005). Impact of the carbon coating thickness on the electrochemical performance of $LiFePO_4$/C composites. *Journal of the Electrochemical Society*, 152(3), A607.

[21] Oh, S. M., Oh, S. W., Yoon, C. S., Scrosati, B., Amine, K., & Sun, Y. K. (2010). High-performance carbon-$LiMnPO_4$ nanocomposite cathode for lithium batteries. *Advanced Functional Materials*, 20(19), 3260-3265.

[22] Moriguchi, I., Hidaka, R., Yamada, H., Kudo, T., Murakami, H., & Nakashima, N. (2006). A Mesoporous Nanocomposite of TiO_2 and Carbon Nanotubes as a High-Rate Li-Intercalation Electrode Material. *Advanced materials*, 18(1), 69-73.

[23] Rolison, D. R., Long, J. W., Lytle, J. C., Fischer, A. E., Rhodes, C. P., McEvoy, T. M., ... & Lubers, A. M. (2009). Multifunctional 3D nanoarchitectures for energy storage and conversion. *Chemical Society Reviews,* 38(1), 226-252.

[24] Long, J. W., Dunn, B., Rolison, D. R., & White, H. S. (2004). Three-dimensional battery architectures. Chemical Reviews, 104(10), 4463-4492.

[25] Zu, C. X., & Li, H. (2011). Thermodynamic analysis on energy densities of batteries. *Energy & Environmental Science,* 4(8), 2614-2624.

[26] Padhi, A. K., Nanjundaswamy, K. S., & Goodenough, J. B. (1997). Phospho‐olivines as positive‐electrode materials for rechargeable lithium batteries. *Journal of the electrochemical society*, 144(4), 1188.

[27] Ohzuku, T., Ueda, A., & Yamamoto, N. (1995). Zero-strain insertion material of Li $[Li_{1/3}Ti_{5/3}]O_4$ for rechargeable lithium cells. *Journal of the Electrochemical Society*, 142(5), 1431.

[28] Winter, M., & Besenhard, J. O. (1999). Electrochemical lithiation of tin and tin-based intermetallics and composites. *Electrochimica Acta*, 45(1-2), 31-50.

[29] Chen, J. S., & Lou, X. W. D. (2012). SnO_2 and TiO_2 nanosheets for lithium-ion batteries. *Materials Today*, 15(6), 246-254.

[30] Yang, H. G., Liu, G., Qiao, S. Z., Sun, C. H., Jin, Y. G., Smith, S. C., ... & Lu, G. Q. (2009). Solvothermal synthesis and photoreactivity of anatase TiO_2 nanosheets with dominant {001} facets. *Journal of the American Chemical Society*, 131(11), 4078-4083.

[31] Han, X., Kuang, Q., Jin, M., Xie, Z., & Zheng, L. (2009). Synthesis of titania nanosheets with a high percentage of exposed (001) facets and related photocatalytic properties. *Journal of the American Chemical Society*, 131(9), 3152-3153.

[32] Liu, J., Chen, J. S., Wei, X., Lou, X. W., & Liu, X. W. (2011). Sandwich‐like, stacked ultrathin titanate nanosheets for ultrafast lithium storage. *Advanced Materials*, 23(8), 998-1002.

[33] Yun, S., Si, Y., Shi, J., Zhang, T., Hou, Y., Liu, H., ... & Hagfeldt, A. (2020). Electronic Structures and Catalytic Activities of Niobium Oxides as Electrocatalysts in Liquid‐Junction Photovoltaic Devices. *Solar Rrl*, 4(3), 1900430.

[34] Lou, L., Kong, X., Zhu, T., Lin, J., Liang, S., Liu, F., ... & Pan, A. (2019). Facile fabrication of interconnected-mesoporous T-Nb_2O_5 nanofibers as anodes for lithium-ion batteries. *Science China Materials,* 62(4), 465-473.

[35] Yan, L., Rui, X., Chen, G., Xu, W., Zou, G., & Luo, H. (2016). Recent advances in nanostructured Nb-based oxides for electrochemical energy storage. *Nanoscale*, 8(16), 8443-8465.

[36] Lou, S., Cheng, X., Ma, Y., Du Chunyu, G. Y., & Yin, G. (2015). Nb-based oxides as anode materials for lithium ion batteries. *Progress in Chemistry*, 27(2/3), 297.

[37] Lv, Z., Meng, W., Yang, Y., Zhang, Y., Ye, M., & Li, C. C. (2021). Nb-based compounds for rapid lithium-ion storage and diffusion. *Journal of Power Sources*, 496, 229840.

[38] Griffith, K. J., Seymour, I. D., Hope, M. A., Butala, M. M., Lamontagne, L. K., Preefer, M. B., ... & Grey, C. P. (2019). Ionic and electronic conduction in TiNb2O7. *Journal of the American Chemical Society*, 141(42), 16706-16725.

[39] Wang, G., Wen, Z., Du, L., Yang, Y. E., Li, S., Sun, J., & Ji, S. (2017). Hierarchical Ti-Nb oxide microspheres with synergic multiphase structure as ultra-long-life anode materials for lithium-ion batteries. *Journal of Power Sources*, 367, 106-115.

[40] Guo, B., Yu, X., Sun, X. G., Chi, M., Qiao, Z. A., Liu, J., ... & Dai, S. (2014). A long-life lithium-ion battery with a highly porous $TiNb_2O_7$ anode for large-scale electrical energy storage. *Energy & Environmental Science*, 7(7), 2220-2226.

[41] Yu, H., Cheng, X., Zhu, H., Zheng, R., Liu, T., Zhang, J., ... & Shu, J. (2018). Deep insights into kinetics and structural evolution of nitrogen-doped carbon coated $TiNb_{24}O_{62}$ nanowires as high-performance lithium container. *Nano Energy*, 54, 227-237.

[42] Shen, L., Wang, Y., Lv, H., Chen, S., van Aken, P. A., Wu, X., ... & Yu, Y. (2018). Ultrathin $Ti_2Nb_2O_9$ nanosheets with pseudocapacitive properties as superior anode for sodium-ion batteries. *Advanced Materials*, 30(51), 1804378.

[43] Osada, M., Takanashi, G., Li, B. W., Akatsuka, K., Ebina, Y., Ono, K., ... & Sasaki, T. (2011). Controlled Polarizability of One-Nanometer-Thick Oxide Nanosheets for Tailored, High-κ Nanodielectrics. *Advanced Functional Materials*, 21(18), 3482-3487.

[44] Yuan, H., Dubbink, D., Besselink, R., & ten Elshof, J. E. (2015). The Rapid Exfoliation and Subsequent Restacking of Layered Titanates Driven by an Acid–Base Reaction. *Angewandte Chemie,* 127(32), 9371-9375.

[45] Lu, F., Chen, Q., Geng, S., Allix, M., Wu, H., Huang, Q., & Kuang, X. (2018). Innovative lithium storage enhancement in cation-deficient anatase via layered oxide hydrothermal transformation. *Journal of Materials Chemistry A*, 6(47), 24232-24244.

[46] Choi, N. S., Chen, Z., Freunberger, S. A., Ji, X., Sun, Y. K., Amine, K., ... & Bruce, P. G. (2012). Challenges facing lithium batteries and electrical double‐layer capacitors. *Angewandte Chemie International Edition,* 51(40), 9994-10024.

[47] Yamada, Y., Iriyama, Y., Abe, T., & Ogumi, Z. (2009). Kinetics of electrochemical insertion and extraction of lithium ion at SiO. *Journal of The Electrochemical Society*, 157(1), A26.

[48] AJ, B., & Faulkner, L. R. (1980). Electrochemical methods: Theory and applications.

[49] Kim, H. S., Cook, J. B., Lin, H., Ko, J. S., Tolbert, S. H., Ozolins, V., & Dunn, B. (2017). Oxygen vacancies enhance pseudocapacitive charge storage properties of MoO_{3-x}. *Nature materials*, 16(4), 454-460.

[50] Augustyn, V., Come, J., Lowe, M. A., Kim, J. W., Taberna, P. L., Tolbert, S. H., ... & Dunn, B. (2013). High-rate electrochemical energy storage through Li+ intercalation pseudocapacitance. *Nature materials*, 12(6), 518-522.

[51] Lindström, H., Södergren, S., Solbrand, A., Rensmo, H., Hjelm, J., Hagfeldt, A., & Lindquist, S. E. (1997). Li+ ion insertion in TiO2 (anatase). 2. Voltammetry on nanoporous films. *The Journal of Physical Chemistry B,* 101(39), 7717-7722.

Appendix A Reference XRD data for $H_3Ti_5NbO_{14}$

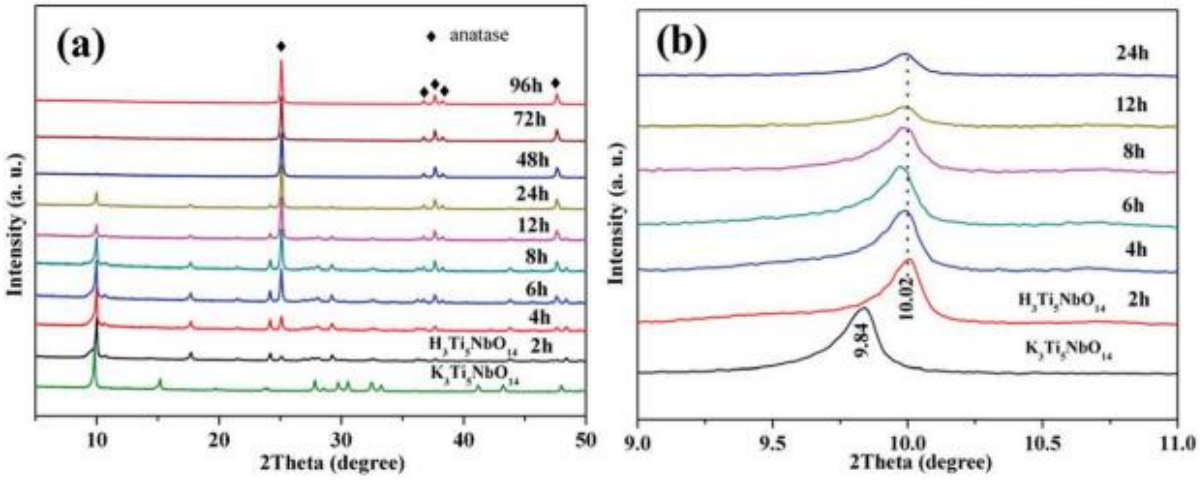

Figure A.5.1 XRD patterns of $K_3Ti_5NbO_{14}$ and the products from the hydrothermal reactions at 180°C with 0.5 M acetic acid for various reaction durations: (b) enlargement of (a) in the 9–11° 2Θ range.[45]